PARTICLE DEPOSITION MODEL FOR A FULLY DEVELOPED TURBULENT CHANNEL FLOW

A Thesis

by

KHOI MINH NGO

Submitted to the Graduate and Professional School of
Texas A&M University
in partial fulfillment of the requirements for the degree of

MASTER OF SCIENCE

Chair of Committee,	N. K. Anand
Committee Members,	Yassin Hassan
	Mark Kimber
Head of Department,	Guillermo Aguilar

May 2023

Major Subject: MECHANICAL ENGINEERING

ABSTRACT

"Plate-out" refers to the deposition or buildup of solid material on a surface, which can have consequences such as increasing the risk of criticality or corrosion and the efficiency of equipment and systems. Current plate-out codes predicting fission products and graphite dust transport are only accessible for internal institutional use and are solely applicable to the nuclear application, despite the fact that porous particle deposition is a crucial component of many industrial heat recovery systems. The numerical findings based on the original geometry may be imprecise due to the accumulating deposition. This study aims to develop a mathematical model for particle deposition under a fully-developed turbulent flow in a rectangular channel, taking the effect of the change in geometry over time. The most significant part of the model is mathematically predicting the equilibrium thickness/mass of the deposition. Non-dimensionalization, scaling analysis, and parametric study are conducted and reported. For a fixed free stream velocity, the critical friction velocity decreases for larger particles. Critical frictional velocity is the velocity at which the deposited particles on a surface begins to lift off. For a fixed particle diameter, the critical friction velocity decreases as the free stream velocity increases. For a fixed Reynolds number Re, as the non-dimensional particle relaxation time increases, the particles take longer time to adjust themselves back to the fluid streamlines, resulting in higher possibility of being deposited on the wall. Hence, the non-dimensional deposition velocity increases with an increase in non-dimensional particle relaxation time. For a fixed Re, as particle relaxation time increases, the deposition velocity increases, resulting in more particles being deposited over a unit area and time. In general, as more particles are deposited, the surface takes less time to become saturated and approach equilibrium faster. Therefore, the saturation and equilibrium time decrease with an increase in non-dimensional particle relaxation time. For a fixed particle concentration, as the inlet velocity increases, the saturation and equilibrium time decreases, and the asymptotic deposited mass decreases.

DEDICATION

With all my heart, I want to dedicate this thesis to my beloved parents, who sacrificed everything they had to ensure I made it to the end of my education journey. Their unwavering support, tireless efforts, and unyielding encouragement made this project a reality, and I am forever grateful for their boundless love and sacrifices. Without them, I would never have made it to this point, and their contributions will always be cherished and remembered.

ACKNOWLEDGMENTS

I want to take a moment to express my deepest gratitude to the people who have made this achievement possible. First and foremost, I owe a debt of gratitude to my advisor, Dr. N. K. Anand. His unwavering support, expert guidance, and invaluable advice have been a constant source of inspiration throughout this entire project. Dr. Anand's mentorship has been instrumental in getting me to where I am today, and I will always be thankful for his influence on my academic and professional journey. His commitment to each student's personal development was a motivating factor in my decision to pursue a Master's degree.

I also want to extend my appreciation to Dr. Yassin Hassan, who allowed me to work as an undergraduate student technician at the Thermal-hydraulic Research Laboratory. The skills I developed during my time in this position have been invaluable and carried with me as I'm transitioning to my career.

Lastly, I want to thank Dr. Mark Kimber for all MatLab coding assignments in NUEN302 and the unforgettable introduction to Computation Fluid Dynamic in NUEN489. The techniques, knowledge, and tools that I gained through these courses were the crucial foundation for my research and professional work later on. Dr. Kimber's passion and expertise in his field have inspired me to strive for excellence in my endeavors.

CONTRIBUTORS AND FUNDING SOURCES

Contributors

I express my gratitude to General Atomics, Idaho National Laboratory, and X-Energy for their valuable inputs that have significantly aided my work.

Funding Sources

This thesis has been financially supported by US Department of Energy (DE-NE009131).

NOMENCLATURE

HTGR	High-temperature gas cooled reactor
FPs	Fission products
IHX	Intermediate heat exchanger
LBM	Lattice Boltzmann Method
MRT	Multiple relaxation time
FVM	Finite Volume Method
CFD	Computational Fluid Dynamic
u_d^+	Non-dimensional deposition velocity
u_d	Deposition velocity, $particles/m^2.s$
Sc	Schmidt number
ν_f	Kinematic viscosity of working fluid, m^2/s
ρ_f	Density of working fluid, kg/m^3
μ_f	Dynamic viscosity of working fluid, $kg/m.s$
d_p	Particle diameter, m
r_p	Particle radius, m
ρ_p	Particle density, kg/m^3
T	Temperature, K
t	Time, s
τ^+	Nondimensional particle relaxation time
τ	Particle relaxation time, s
U	Velocity, m/s
$V_{freestream}$	Free stream velocity, m/s

V_{inlet}	Inlet velocity, m/s
h	Channel radius, m
u^*	Friction (or shear) velocity, m/s
g^+	Non-dimensional gravitational acceleration
g	Gravitational acceleration, m/s^2
Re	Reynolds number
Re_p	Particle Reynolds number
J_N	Particle flux, $particle/m^2.s$
J_m	Mass flux, $kg/m^2.s$
$J_{N,A}$	Number of particles deposited over a certain area, $particle/m^2$
m_{dep}	Mass deposited, kg
A	Area, m^2
t_{sat}	Saturation time, s
t_{eq}	Equilibrium time, s
t^+_{sat}	Nondimensional saturation time
δ_c	Equilibrium thickness, m
m_{eq}	Equilibrium mass, kg
m_f	Fluid mass, kg
M_t	Hydrodynamic torque, Nm
C_c	Cunningham correction factor
C_d	Correction factor to account for the Stokes drag at high velocities
F_t	Drag force, N
F_l	Lift force, N
F_c	Impact force, N

F_{po}	Total adhesion force, N
$F_{gravity}$	Gravitational force, N
$F_{electrostatic}$	Electrostatic force, N
F_{vDW}	Van der Waals force, N
L_c	Characteristic length, m
C_0	Particle concentration $particles/m^3$
Stk	Stokes number
f	Friction factor
z_0	Separation distance between the particle and the substrate, m
A_H	Hamaker's constant, J
a	Non-vanishing contact radius, m
E	Young's modulus, N/m^2
E^*	Effective Young's modulus, N/m^2
m^*	Effective mass, kg
r^*	Effective radius, m
V_{cl}	Impacting velocity, m/s
K	Composite Young's modulus, N/m^2
γ	Poisson's ratio
k	Spring constant, N/m
q	Charge, $Coulomb$
ϵ	Dielectric constant

TABLE OF CONTENTS

Page

LIST OF FIGURES

FIGURE Page

LIST OF TABLES

TABLE Page

1. INTRODUCTION

High-temperature gas-cooled reactor (HTGR) is a fourth-generation reactor design that employs graphite-moderated nuclear fuel and helium cooling [1], [2]. During regular reactor operation, interactions between the fuel assembly and graphite moderators produce graphite dust that accumulates on primary loop components. Fission products (FPs) generated during normal operation can also cause the dust to become radioactive [3].

The deposition of "condensable" FPs on helium-wetted surfaces under normal operating conditions is known as "plate-out". FPs released from fuel elements have determined reactor thermal-hydraulic conditions, physico-chemical interactions of Helium (He) gas coolant, fission gases such as Krytpton (Kr), Xenon (Xe), Iodine (I), Cesium (Cs), and impurities including water, carbonaceous dust, and metallic materials. A plate-out activity represents all deposition regardless of the physico-chemical mechanisms involved, such that FPs can deposit on various structural surfaces, flow dead zones in the primary loop, or previously deposited particulates. The graphite structures inside the reactor vessel capture 86% of the generated dust, while the remaining dust is collected in the primary system's connecting pipes and high-temperature intermediate heat exchanger (IHX), with residual dust accumulating in the low-temperature IHX [3].

The radioactive FPs may cause operational issues and negatively impact the reactor's stability and safety [4]. Accumulated radioactive graphite dust in heat exchangers may reduce heat transfer rates and complicate system inspection, maintenance, and repair [5]. In pipeline breaks that cause depressurization accidents, deposited graphite dust may resuspend and contaminate the environment with radioactive FPs [6]. Therefore, investigations into all transport mechanisms and activities of graphite dust and FPs are necessary for the safe and reliable operation of HTGRs.

2. LITERATURE REVIEW, RESEARCH OPPORTUNITIES, AND OBJECTIVE

2.1 Current plate-out codes

“Plate-out" refers to the deposition or accumulation of solid material on a surface, usually caused a physical process. In the context of nuclear power, plate-out could refer to the accumulation of radioactive particles or substances on surfaces within the reactor or containment system. Plate-out can have consequences such as increasing the risk of criticality or corrosion and can also affect the efficiency of equipment and systems. To evaluate the steady-state and time-dependent plateout of fission products in any network of pipes, a one-dimensional computer software Plateout Activity Distribution for Loss of Circulation (PADLOC) was created [7]. The effects of sources in the fluid and on the plateout surfaces, convection along the flow paths, decay, adsorption on surfaces (plateout), and desorption from surfaces are examples of related phenomena. They are modeled by linearizing the governing equations about an approximate solution, using the Newton-Raphson iteration technique, the finite difference solution method with an implicit time integration, and the substructuring technique to logically arrange the systems of equations for an arbitrary flow network. Plate-out Analysis program based on Iniotakis model (PLAIN) code uses coupled set of six linear differential equations [8]. Many unknown coefficients in PLAIN remained unidentified because they were solely based on the Japan Atomic Energy Agency (JAEA) database. The relevance of the coefficients to the other datasets needs to be clarified. There are no published studies that validate utilizing U.S. data [9]. Adsorption-desorption behavior and mass transfer were combined and developed in Germany, SPATRA [10]. The desorption enthalpies were calculated from multiple deposition experiments and were only applicable to surface layers with low FPS fractional coverage [11]. RADAX was developed during the 1980s for Germany’s High-temperature Helium Turbine (HHT) project [12]. RADAX’s fundamental plate-out model is comparable to other alternative codes such as SPATRA. RADAX simulates the following transport processes: Aerosol particle deposition, migration of fission products in wall materials, deposition of atomic/molecular

condensable fission products to the surfaces of the primary power system components, and resuspension of deposited aerosol particles during depressurization events [13]. The current approaches to estimating the fission product plate-out behavior in a gas-cooled system are well-acknowledged to contain significant uncertainty [14]. The GAMMA-FP algorithm was previously created by the Korea Atomic Energy Research Institute (KAERI) utilizing the one-dimensional model for the fission product plateout [14], [15]. However, due to inadequate computational efficiency, GAMMA-FP was shown to have serious limits for the simulation over a lengthy time (e.g., 20–60 years) [16]. For the primary circuit of an HTGR, a new computer program called Plate-Out Surface and Circulating Activities (POSCA) was created to assess the fission product plateout and circulating coolant activities. The POSCA code uses a one-dimensional model, whereas a different computational strategy was used to improve GAMMA-subpar FP's computational performance [9]. However, using these models may be challenging due to several inherent unknowns from FPs' properties, using the models may be challenging. Specifying the unknowns for each base metal and fission product requires much effort and a systematic approach.

2.2 Research Opportunities

The majority of existing plate-out models assume that the contacting surfaces operate as a perfect sink and do not consider the fact that the geometries of the deposition layer continue to change during deposition. They are also only accessible for internal institutional use. The deposition rate is further impacted by the deposition layer, which alters the flow characteristics. The numerical findings based on the original geometry may be imprecise due to accumulating deposition [17]. Although porous particle deposition is a critical component of many industrial heat recovery systems because it greatly reduces the heat transfer coefficient and impairs performance, these codes only apply to nuclear applications. [18]–[20].

The deposition layer's development and form were taken into consideration in several studies. The shape and size of the depositions on platen super heaters in pulverized coal boilers were modeled by Tomeczek and Wacawiak [21]. The tube spacing bridging phenomenon was observed in the simulation, and the impacts of particle size were investigated. Additionally, Paz et al. created

a CFD model to represent the fouling of diesel exhaust systems [22]. The experiment and expected fouling on a tube were compared. However, the exact deposition mechanisms were not considered because the deposition model utilized in these simulations was based on sticking probabilities. In the study of deposition processes, the deposition mechanism and the development of the deposition layer should be considered. A numerical technique integrating the multiple-relaxation-time lattice Boltzmann method (MRT-LBM) and the finite volume method (FVM) was proposed to model the fouling processes on tubes [17]. The LBM is a practical and versatile approach for multi-physio-chemical phenomena in complicated changing geometries due to its particulate nature [23], [24]. The LBM might be used to mimic snow transport, erosion, deposition patterns, and the scour that forms around an underwater pipe in terms of particle motion and deposition [25]–[27]. The model contained detailed particle deposition and removal procedures, and the development of the fouling layers over time was achieved. The force and moment analysis was used to determined the particle removal. Tong et al. discovered that the fouling area increases linearly with time without a removal mechanism. The fouling area increases exponentially and reaches an asymptotic value when the removal method is considered [17]. The detail on the asymptotic value of fouling has yet to be documented. Simulation combining MRT-LBM and FVM has not been experimentally validated.

2.3 Objective

The objective of this study is to develop a mathematical model for particle deposition under a fully-developed, turbulent channel flow without the use of internal institutional codes. The study will introduce deposition velocity, asymptotic deposition model, particle removal mechanism by analyzing all forces and moments acting on each particle. An iterative scheme to mathematically predict the critical friction velocity and the equilibrium thickness of the particle deposition is also presented. Lastly, non-dimensionalization, scaling analysis and parametric study were conducted and results are reported. The study will give an introduction to Atomic Force Microscopy and the proposed experiment to measure the total adhesion force acting on the particle as the parameter is crucial in estimating the critical friction velocity and the equilibrium thickness.

3. MODEL DEVELOPMENT

3.1 Wood's deposition velocity model

Plate-out transport mechanisms consist of: deposition, nuclear decay, and absorption. Nuclear decay and absorption are beyond the scope of this study. Hence, the deposition will be the main topic of discussion. Particulate deposition is defined as the accumulation of particles onto the surface of an adsorbent by various mechanisms. Wood's model [28] for empirically estimating a non-dimensional particle deposition velocity u_d^+ in turbulent flows is given as follows:

$$u_d^+ = 0.057Sc^{-2/3} + 4.5 \times 10^{-4}\tau^{+2} + \tau^+ g^+. \tag{3.1}$$

The first term, Schmidt number Sc, numerically describes the effect of Brownian diffusion as:

$$Sc = \frac{\nu_f}{D_p}. \tag{3.2}$$

where ν_f is the working fluid kinematic viscosity and D_p is particle diffusivity determined as:

$$D_p = \frac{kT}{3\pi\mu_f d_p}. \tag{3.3}$$

In Equation 3.3, k is the Boltzmann's constant and T is the absolute temperature. The second term describes the effect of eddy-impaction. τ_p^+ is the non-dimensional particle relaxation time determined from the friction velocity u^*:

$$\tau_p^+ = \frac{d_p^2 u^{*2}\rho_p}{18\nu_f^2\rho_f}. \tag{3.4}$$

The third term describes the effect of gravitational sedimentation. The non-dimensional acceleration g^+ due to gravity was defined as:

$$g^+ = \frac{\nu_f g}{u^{*3}}. \tag{3.5}$$

Chavez et al in his experiment to validate the Wood's model at various non-dimensional relaxation time and Reynolds number showed that a reduction in the deposition velocity was observed with an increase in particle relaxation time [29]. In their experimental study, the authors also observed that gravitation sedimentation strongly influenced on the particle deposition for Re = 3,500; 5,000; and 6,500. As the particle diameter decreases for a given flow velocity, gravitational sedimentation plays a larger role in particle deposition because of reduced relaxation time. An increase in the Reynolds number for a given particle diameter resulted in an increase in the particle relaxation time but a decrease in the particle deposition velocity.

Particle flux at the wall ($Particles/m^2.s$) is calculated using free stream aerosol concentration C_0 and friction velocity u^* as:

$$J_N = u_d^+ u^* C_0. \tag{3.6}$$

Mass flux at the wall ($kg/m^2.s$) is calculated from particle's mass as:

$$J_m = m_{part} J_N. \tag{3.7}$$

Total mass deposited over a certain period of time and area without removal mechanism was proposed as:

$$m_{dep} = J_m A t. \tag{3.8}$$

The number of particles deposited over a certain area per unit time as:

$$J_{N,A} = J_N A. \tag{3.9}$$

3.2 Asymptotic deposition model and mathematical development

According to the well-known asymptotic deposition model, removal will take place over a certain period of time as the hydraulic diameter changes, and the mass accumulated will not be linearly increasing anymore. In this study, it is defined as under-saturated when the removal rate is negligible compared to the deposition rate. It is defined as saturated when the removal rate become

large and considerable compared to the deposition rate. Saturation time t_{sat} is defined as when the transition between under-saturated and saturated occurs. The particles gradually build up layers, whose thickness increases over time after being saturated until an equilibrium is established. Equilibrium region is determined when deposition and removal rates are equal. The deposition grows linearly with time without removal mechanism. When the removal mechanism is considered, the thickness grows exponentially and reaches an asymptotic value in a form of an exponential function $F = X(1 - e^{-Bt})$ [17]. Under-saturated, saturated, equilibrium region and asymptotic behavior are graphically presented in Figure 3.1. Equilibrium time t_{eq} is defined when the deposition has reached 99% of the asymptotic deposited mass. The suggested asymptotic deposition model is consistent with the one mentioned in [30].

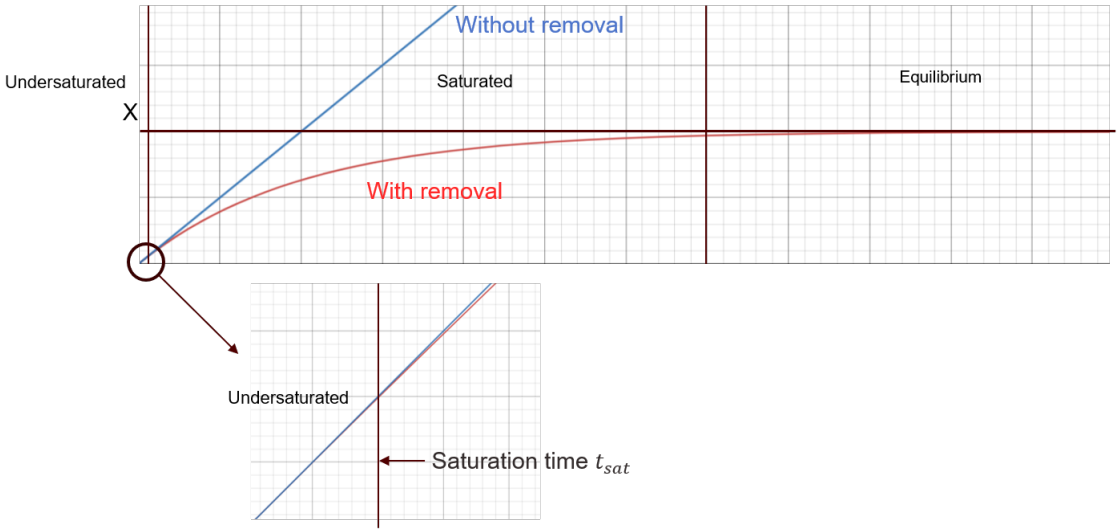

Figure 3.1: Asymptotic deposition model.

As deduced from all studies presented, to model the exponential function, define the diffusion thickness at equilibrium as δ_c. The volume of the equilibrium thickness over a deposition area A is:

$$V_c = \delta_c A. \tag{3.10}$$

Since the deposition particle is considered as porous media, a three-dimensional porosity ϵ_{3D} is also considered when calculating the mass at the equilibrium state:

$$m_{eq} = V_a c \rho_{part}(1 - \epsilon_{3D}). \tag{3.11}$$

Consider the deposited mass as a function of time is in the form of exponential function $m(t) = A(1 - e^{-Bt})$, where X is the maximum value (mass), and B is a time constant. Because the mass does not change at the equilibrium state, it can be concluded that the mass at the equilibrium state can be substituted as X:

$$m(t) = m_{eq}(1 - e^{-Bt}). \tag{3.12}$$

Taylor series expansion of the exponential form about $t = 0$ is given as follows:

$$m(t) = m_{eq}(Bt - \frac{B^2t^2}{2} + \frac{B^3t^3}{6} - O(t^4)). \tag{3.13}$$

The exponential form and the linear form start diverging at t_{sat}. The Equation 3.13 can be written as follows:

$$m(t_{sat}) = m_{eq}(Bt_{sat} - \frac{B^2t_{sat}^2}{2} + \frac{B^3t_{sat}^3}{6} - O(t_{sat}^4)). \tag{3.14}$$

Because the mass deposited over a certain period of time and area without removal mechanism was proposed in Equation 3.8:

$$J_m A t_{sat} = m_{eq}(Bt_{sat} - \frac{B^2t_{sat}^2}{2} + \frac{B^3t_{sat}^3}{6} - O(t_{sat}^4)). \tag{3.15}$$

Dividing both sides by $t_{sat} \times m_{eq}$ yields::

$$\frac{J_m A}{m_{eq}} = B - \frac{B^2 t_{sat}}{2} + \frac{B^3 t_{sat}^2}{6}. \tag{3.16}$$

Because the exponential and the linear form need to be continuous at t_{sat}, the value and the deriva-

tives have to be equal:

$$\frac{J_m A}{m_{eq}} = B - B^2 t_{sat}^2 + \frac{B^3 t_{sat}^3}{2}. \tag{3.17}$$

Solving a set of two Equations 3.16 and 3.17 yields:

$$t_{sat} = \frac{3}{2B} = \frac{15\delta_c(1-\epsilon_{3D})\rho_{part}}{16 m_{part} J_N}. \tag{3.18}$$

$$B = \frac{8 J_m A}{5 m_{eq}} = \frac{8 m_{part} J_N}{5\delta_c(1-\epsilon_{3D})\rho_{part}} \tag{3.19}$$

The final form of the asymptotic deposition is:

$$m(t) = \delta_c A(1-\epsilon_{3D})\rho_{part}(1 - e^{-\frac{3t}{2t_{sat}}}). \tag{3.20}$$

Equilibrium time t_{eq} is defined when the deposition has reached 99% of the asymptotic deposited mass, which can be predicted from Equation 3.12 by substituting $m(t_{eq}) = 0.99 m_{eq}$, dividing both sides by m_{eq} and solving as a function of time constant B:

$$t_{eq} = -\frac{ln(0.01)}{B}. \tag{3.21}$$

Equilibrium time t_{eq} can be expressed as a linear function of t_{sat} by dividing Equation 3.21 by 3.18, which can be used to approximate one or the other with adequate given parameters. That is:

$$\frac{t_{eq}}{t_{sat}} = -\frac{ln(0.01)}{3/2} = 3.067. \implies t_{eq} = 3.067 \times t_{sat}. \tag{3.22}$$

3.3 Particle removal mechanism

The final parameter needs solving for the diffusion thickness at equilibrium is δ_c. All forces acting on the particle during removal must be thoroughly investigated. Because the hydraulic diameter changes as the diffusion thickness caused by deposition accumulate over time, the shear stress, Reynolds number, and all other related parameters are now time-dependent. To simplify

the problem statement, consider a case where flow is turbulent and fully developed even when the hydraulic diameter has been altered because of the diffusion thickness at equilibrium. The deposition area is reasonably small; therefore, uniform shear stress profile can be safely assumed. Toscano and Ahmadi (2002) conducted a detailed study on all forces acting on a particle, where effects of particle size, materials (Van der Waals force), hydrodynamic torque, impact force, lift force, and drag force are all considered [31]. A free-body diagram of forces acting on an adhered particle, as detailed by Toscano and Ahmadi, is presented in Figure 3.2.

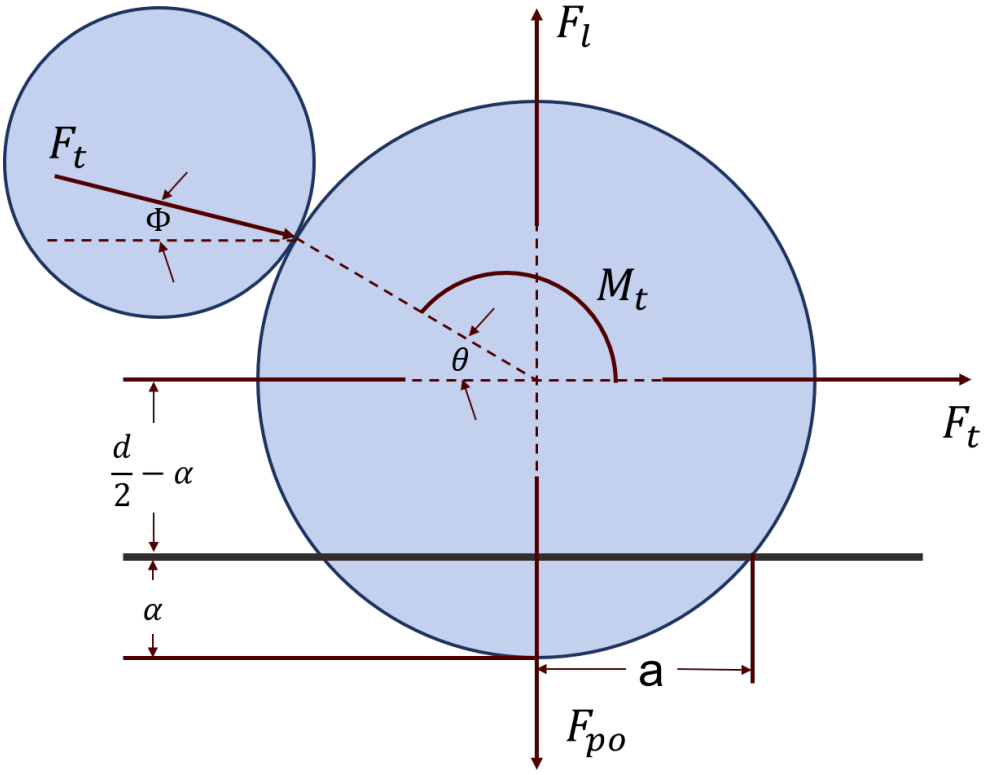

Figure 3.2: Free-body diagram of forces acting on an adhered particle.

Hydrodynamic torque is defined as a function of shear velocity as:

$$M_t = \frac{1.07\pi\rho_f d^3 u^{*2}}{C_c}. \tag{3.23}$$

with C_c is the Cunningham correction factor calculated from the particle diameter d_1 and mean free path of the fluid λ:

$$C_c = 1 + \frac{2\lambda}{d_1}(1.257 + 0.4e^{\frac{-1.1d}{2\lambda}}). \tag{3.24}$$

The drag force is defined as a function of shear velocity as:

$$F_t = \frac{2.9\pi\rho_f d^2 u^{*2} C_d}{C_c}. \tag{3.25}$$

with C_d is the correction factor to account for the Stokes drag at high velocities calculated from the particle's Reynolds number Re_p:

$$C_d = 1 + 0.15Re_p^{0.689}. \tag{3.26}$$

$$Re_p = \frac{u^* d}{\nu_f}. \tag{3.27}$$

The lift force is given by

$$F_l = 0.915\rho_f \nu_f^2 Re_p^3. \tag{3.28}$$

The impact force between two particles is given as:

$$F_c = 1.28E^{*2/5} r^{*1/5} m^{*3/5} V_{cl}^{6/5}. \tag{3.29}$$

with V_{cl} is an impacting velocity between particles and is assumed to be equal to the freestream velocity $V_{freestream}$ in this study. Toscano and Ahmadi (2002) also indicated that the impaction between particles is the primary removal mechanism [31]. The contact modulus is the effective Young's modulus E^* for interactions between the adhered (subscript 1) and colliding particles (subscript 2), which is given as Poisson's ratio γ:

$$E^* = \left(\frac{1-\gamma_1^2}{E_1} + \frac{1-\gamma_2^2}{E_2}\right)^{-1}. \tag{3.30}$$

The effective radius r^* is defined as the inverse mean of the two radii and is given by:

$$r^* = \left(\frac{1}{r_1} + \frac{1}{r_2}\right)^{-1}. \tag{3.31}$$

The effective mass m^* is also the inverse mean of the two particles and is given by:

$$m^* = \left(\frac{1}{m_1} + \frac{1}{m_2}\right)^{-1}. \tag{3.32}$$

Van der Waal force is generally considered as the primary adhesion force between the particles and solid surfaces under dry and electrically neutral atmospheric settings [32], [33]. Details about adhesion force and the total adhesion force with its constituents will be further investigated in Section 3.4.1. The van der Waals force between a spherical particle and a flat surface can be expressed by the following equation:

$$F_{vDW} = \frac{A_H d_p}{12 z_0^2}. \tag{3.33}$$

W_A is defined as the thermodynamic work of adhesion, the lowest possible work required to separate a joint between two surfaces from each other:

$$W_A = \frac{A_H}{12\pi z_0^2}. \tag{3.34}$$

z_0 is the minimum separation distance, which is widely used as 0.35 nm, and A_H is a Hamaker's constant from the material. According to the JKR theory [34], at the moment of separation, there is a non-vanishing contact radius when there is no external force applied to the particle, a, which is given as:

$$a = \left(\frac{3\pi W_A d_1^2}{8K}\right)^{1/3}. \tag{3.35}$$

and the composite Young's modulus, K, between the adhered particle and the particle layer under-

neath is given by:

$$K = \frac{4}{3}E^*. \tag{3.36}$$

In reality, the total adhesion force, F_{po}, will be affected by additional forces, such as gravitational force, the capillary force caused by relative humidity during the operating condition, the electrostatic force caused by the random interactions between particles, particles to fluid, and particles to the wall. Exact mathematical prediction using various methods is not applicable in this study because of the lack of material-specific parameters, specifically Hamaker's constant from the material, electrostatic force, and capillary force. These forces become increasingly significant for fine particles because the particle adhesion force per unit mass increases sharply as the particle size decreases. Alternatively, instead of finding the exact predictions, an experiment using Atomic Force Microscope (AFM) needs to be conducted to measure the total adhesion force, where van der Waals, gravitational capillary, electrostatic and capillary forces are all included. The final measurements will be used in the detachment criteria below. Detail study on adhesion force measurement will be presented in Section 3.4.

3.4 Adhesion force

3.4.1 Fundamentals of Particle Adhesion

The adhesion of dust particles on solid surfaces is governed by several forces, including capillary forces, van der Waal, electrostatic, and gravitational [32], [35]–[37].

3.4.1.1 Capillary force

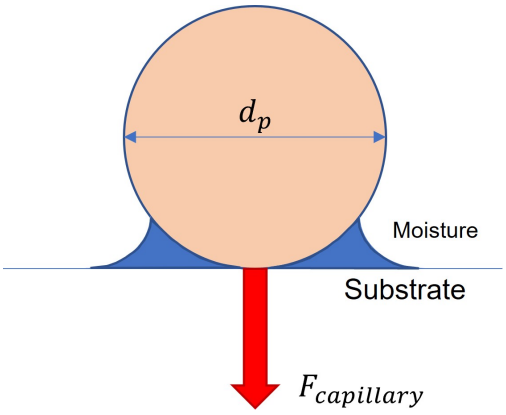

Figure 3.3: Capillary force acting on a deposited particle.

When there is moisture in the environment, capillary forces dominate adhesion (Figure 3.3). Moisture causes the particles to stick to the surface through capillary action. Specifically for larger particles (diameter greater than 10 μm), the capillary force is strong and inversely related to particle diameter [37]. This phenomenon may be seen in particle adherence to glass surfaces, where the adhesion force tends to grow gradually with RH up to a critical point, usually between 60% and 70% RH, before increasing abruptly [36]–[38]. Rabinovich et al (2002) expressed capillary force to include the effect of the relative humidity as the following equation [39]:

$$F_{capillary} = 4\pi r_p \gamma \cos\theta \left(1 - \frac{z_0}{2r\cos\theta}\right). \tag{3.37}$$

where r_p is particle radius, γ is the surface tension, z_0 is the separation distance (0.35 nm), θ is contact angle, and r is the equilibrium radius of meniscus, given by Kelvin's equation [39] as:

$$r = -\frac{M\gamma}{N_a kTln(RH)} \tag{3.38}$$

where M is the molecular weight of water (contacting liquid), 18 mL/mol, N_a is Avogadro's number ($6.022 \times 10^{23} atom/mol$), k is Boltzmann's constant ($1.38 \times 10^{\breve{}23} m^2 Kgs^2 K^1$), T absolute temperature (K), and RH is the relative humidity.

Graphite dust used in this study has an average radius of 3.75 μm, surrounding environment has temperature of 302 K, relative humidity of 80%, water–air surface tension of 71.2$\times 10^{-3}$ N/m, contact angle of the water γ of 43°. The capillary force is estimated to be 2197.7 nN.

3.4.1.2 London-van der Waal force

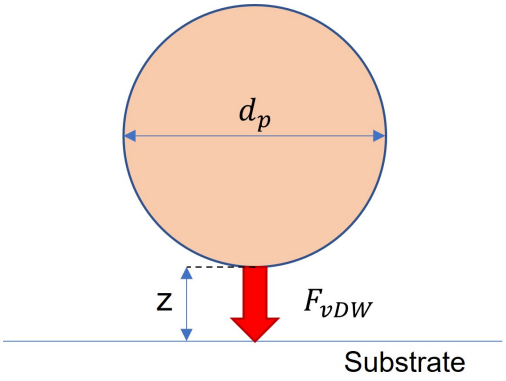

Figure 3.4: Van Der Waal force acting on a deposited particle.

The force that causes any atom or molecule to be drawn to another atom or molecule is known as the London-van der Waal (dispersion) force 3.4 [40]. Van der Waal force may generally be considered as the primary adhesion force between the particles and solid surfaces under dry and electrically neutral atmospheric settings [32], [33]. The van der Waal force between a spherical particle and a flat surface can be expressed by the following equation:

$$F_{vDW} = \frac{A_H d_p}{12 z_0^2}. \tag{3.39}$$

where z_0 is the separation distance between the particle and the flat substrate, R is the radius of the particulate, and A is the Hamaker constant. The parameter z_0 represents the separation

between the particle and the surface [32]. The strength of the van der Waals force is represented by the Hamaker constant, which is influenced by the substrate's materials, particles, and contact medium. The elemental composition of the dominant material in the dust particles must be known to determine the Hamaker constant of the investigated material.

This analysis aims to estimate the adhesion force of graphite dust adhering to a deposited graphite porous substrate. The Hamaker's constant A_H is determined to be 46.9×10^{20} J [41]. The van de Wals force acting on the particle with a diameter of 7.5 μm is estimated to be 2392.9 nN

3.4.1.3 Electrostatic force

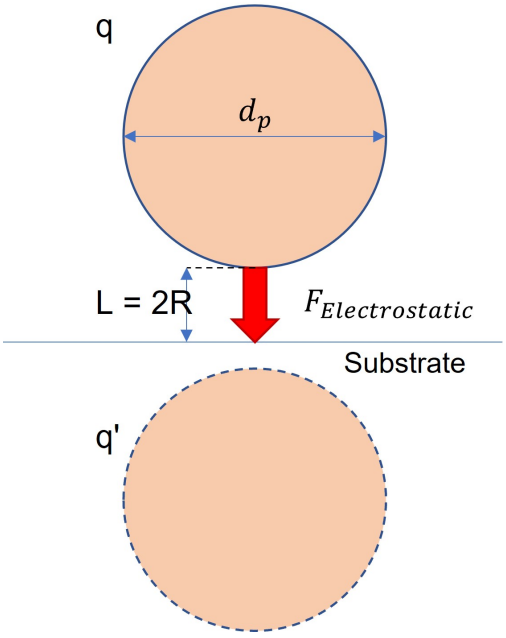

Figure 3.5: Electrostatic force acting on a deposited particle.

Dust particles in the system may acquire an electric charge due to collisions or interactions with working fluids [35]. As flow passes through a channel/object, it experiences frictional forces as it is contacting against the working fluid. Free electrons on the surface are removed, causing the channel/object to build up a net charge. In this study, the metal and porous substrate can build

up a net charge because the contact with the working fluid and free stream particles. Illustration is shown in 3.5. The electrostatic force between a spherical particle and a surface can be expressed by Equation 3.40 as:

$$F_{electrostatic} = \frac{q^2}{4\pi\epsilon\epsilon_0 l^2}. \tag{3.40}$$

where q is the charge of dust particle (C), ϵ is the dielectric constant of the medium between the particle and the surface (for air, $\epsilon = 1$), ϵ_0 is the permittivity of the free space medium (air in this case) and l is the separation distance between the charge centers which is approximately equal to 2 times the radius of the particle [35]. Thus, the electrostatic force is estimated to be 0.026 nN [41].

3.4.1.4 Gravitational force

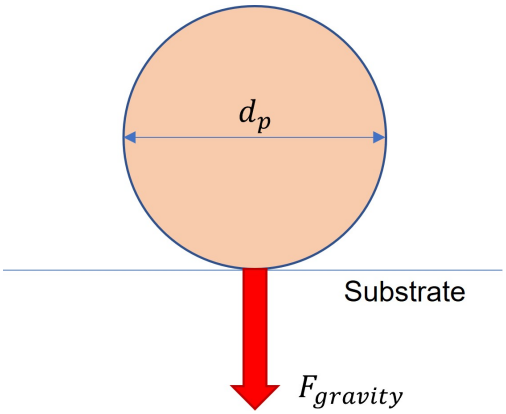

Figure 3.6: Gravitational force acting on a deposited particle.

The gravitational force 3.6 between spherical particle and a substrate is given by:

$$F_{gravity} = \frac{\pi d_p^3 \rho_p g}{6} \tag{3.41}$$

where d_p is the particulate diameter, ρ_p is the density of the particulate's material (2,260 kg/m^3) and g is the gravitational acceleration constant. The gravitational force acting on each particle is found to be 0.00489 nN

The net adhesion force acting on the graphite particle adhered to the graphite porous substrate is a sum of 4 forces, $F_{capillary}$, F_{vDW}, $F_{electrostatic}$, and $F_{gravitational}$.

$$F_{po} = F_{capillary} + F_{vDW} + F_{electrostatic} + F_{gravitational} = 4590.6nN \tag{3.42}$$

3.4.2 Atomic Force Microscope (AFM) experiment

3.4.2.1 Introduction to Atomic Force Microscope (AFM)

In the 1980s, a new method for capturing surface topography at length scales ranging from micrometer to nanoscale was developed using atomic force microscopy (AFM) [42]. AFM can precisely and reliably measure forces in various liquid and gaseous mediums at regulated temperatures. Therefore, AFM is a great method for describing the surface topography of different surfaces and quantitatively analyzing the forces that cause microparticles to adhere to those surfaces [43].

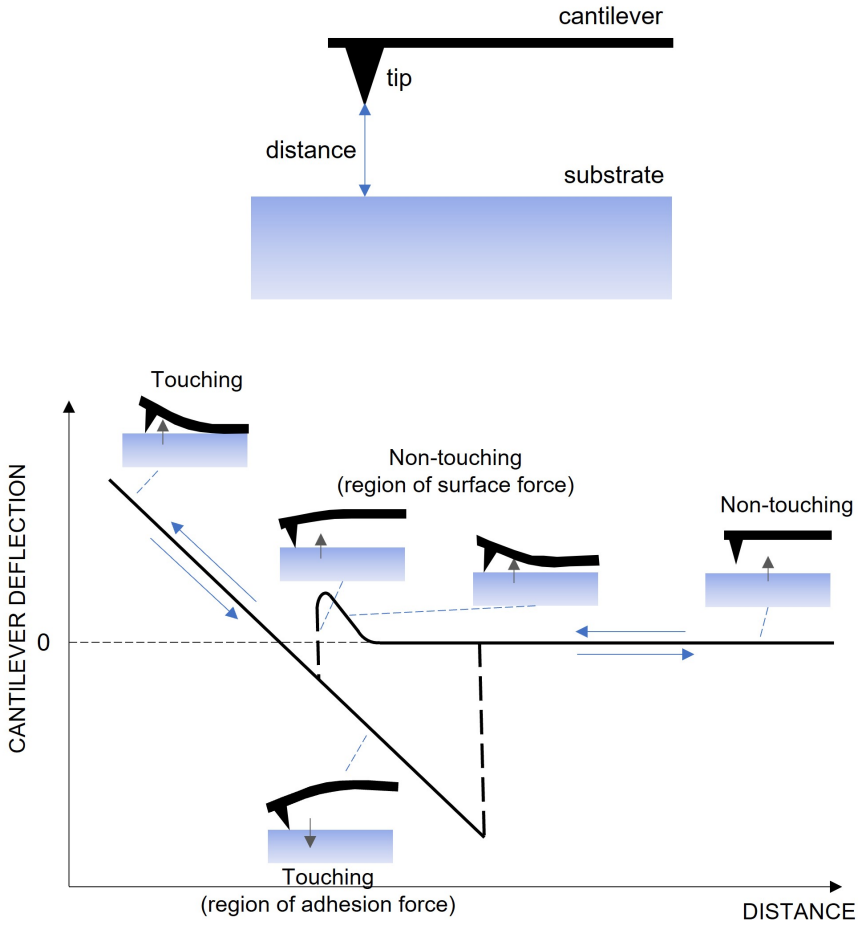

Figure 3.7: Force vs. distance of the cantilever curve in the AFM measurement.

The fundamental idea behind AFM is that a nanoscale tip is attached to a tiny cantilever that acts as a spring. A laser diode and a split photodetector are used to detect the bending of the cantilever when the tip contacts the surface. This bending shows the adhesive force between the tip and the sample. Here, the important aspects of surface force measurements are evaluated. The sharp cantilever tip typically has a radius from 10 to 100 nm, or an attached particle with a diameter typically ranging from about 2 to more than 20 μm and is glued to the end of the cantilever. A laser diode and a split photodetector detect the cantilever's bending as soon as the tip contacts the surface. This bending indicates the force between the tip and the sample. The forces acting between a probing tip and a substrate are related to the deflection measured using a

laser-photodiode system. A schematic of the cantilever deflection vs. tip-substrate distance curves is shown in Figure 3.7, and two cantilever tip examples are shown in Figure 3.8.

Figure 3.8: Graphical illustrations of two cantilever tips used in AFM measurement.

The AFM measurement begins in a nontouching regime at a significant tip-surface separation, as shown in Figure 3.7. The tip then moves toward the surface along the horizontal line that moves from right to left in the force vs. distance curve, either with or without a minor deviation, depending on the long-distance tip-surface interactions. The shift from nontouching to touching takes place, and the tip "jumps" onto the sample surface at a specific point when the tip-substrate interactions overcome the stiffness of the cantilever. As the cantilever is pushed farther through the surface, it deflects by the same amount as the tip's displacement. The diagonal line in the left portion of the force vs. distance curve represents this region, which is known as the touching regime or constant compliance region. The cantilever moves away from the surface when the tip is pulled back, i.e., going toward the right in the force vs. distance curve. Before the tip loses contact with the surface, the cantilever deflects towards the direction of the surface due to adhesion force, passing through the force vs. distance curve's lowest point. The cycle ends when the tip entirely loses contact with the surface at this "jump-off" point. The force required to pull the tip off the substrate surface is determined as total adhesion force (F_{po}) and is calculated from Hooke's law,

$$F_{po} = k\Delta x \tag{3.43}$$

where k is the spring constant of cantilever provided by the manufacturer and Δx is the maximum deflection of the cantilever during tip–substrate adhesion.

Contact mechanic models such JKR [34], DMT [44], Maugis-Dugdale (M-D) [45], and Van der Waals-based models [46], [47] have been consistently tested using AFM force spectroscopy technique with common materials, including silica [48], [49], alumina [50], polystyrene [51], copper [52], gold [53], and stainless steel [54]. However, only limited research has been conducted using the AFM approach to measure the adhesion force between relevant dust and surfaces found in nuclear plants. AFM has only been used in a few investigations between complex-geometry graphite particles and various metal surfaces present in HTRs [24], [55]. To the author's best knowledge, there has not been an attempt to measure the adhesion force between the particles on the top layer and the deposited porous substrate.

A comprehensive understanding and effective implementation of the AFM is of utmost importance due to the existence of a research gap. Toscano and Ahmadi's removal model has been widely used by researchers to forecast the critical shear velocity accurately. However, the original study and related works only consider one of the primary contact mechanics models, JKR, DMT, or Maugis-Dugdale (M-D). Additionally, as presented in Section 3.4.1, there are three other primary forces at work on particles apart from body-body interactions. The particles in the system may acquire an electric charge from collisions with each other or interactions with working fluid. The metal surface and porous substrate can build up a net charge because of the contact with the working fluid and free stream particles. The environment's water-air interaction can cause capillary forces. The aim of this section is to propose an experimental approach to accurately measure the total adhesive force acting on particles adhered to deposited porous substrates. The significant parameters of interest measured through AFM are the total adhesion force from the deposited porous substrate, the total adhesion force from a bare metal substrate, and the work of adhesion. The proposed systematic approach will benefit future research on fission products and graphite dust inside nuclear reactors. This experiment will fill the research gap and help scientists understand the complex behavior of particles in such environments.

3.4.2.2 Sample preparation and experiment description

The particle used is 99.99% pure graphite powder with sizes ranging from 5 μm to 10 μm and an average size of 7.5 μm. The deposited porous substrate is prepared for a long deposition experiment at low temperature and pressure. The sample can be obtained by placing a thin 5mm x 5mm film at the location where the flow is fully developed. The thin film should not be too thick (above 0.5mm) as the thickness will easily alter the flow properties, leading to inaccurate deposition data. Particle concentration is set to 3.27×10^{10} $particles/m^3$, corresponding to a particle injection mass flow rate of 0.000152 kg/s for graphite properties with a hydraulic diameter of 4 inches. Inlet velocity is recommended to be set at 1 to 1.08 m/s to ensure a reasonable run time for the experiment. The deposition behavior is monitored to ensure the sample has reached the asymptotic value.

Cantilevers with attached graphite particles used for AFM experiment are rectangular and made of Silicon, pre-mounted and pre-calibrated to for accurate spring constants by Novascan Technologies, Ames, IA, USA. There are 5 spring constants will be used in this experiment, 0.12 N/m, 0.92 N/m, 1.62 N/m, 2.98 N/m, and 6.2 N/m with a maximum error of 10%. Each cantilever will be mounted with 7.5 μm graphite particles.

The Adhesive force will be measured by Bruker's Dimension AFM-ICON provided by the Materials Characterization Facility at Texas AM University. The tapping mode is selected to reduce shear forces that could harm delicate porous samples. The forces exerted as a function of separation on a single graphite particle attached to the cantilever as a probe will be measured using the AFM apparatus in a regular air environment. The deflection of the cantilever with the graphite probe is monitored and recorded as a function of the displacement of the piezo actuator as the sample is continually moved up and down using laser beam deflection technology. Following the methodology devised by Ducker et al., these cantilever deflection vs. displacement data is converted into reduced force (F/R) vs. separation data [56]. The cantilever deflection rises linearly with decreasing separations, and the zero of force is established at separations where the sample and graphite probe are adequately separated from one another. The zero separation is established

in the constant-compliance region.

3.4.2.3 Proposed experimental procedure

Tip Loading: Begin by placing the cantilever holder onto the cantilever holder stand. Firmly press down and pull the probe clip to the back and insert the tapping mode probe into the groove of the cantilever holder. Secure the cantilever by gently pushing forward the tip holder clip.

Sample Mounting: Mount the sample onto the magnetic discs using double-sided tape.

Camera Alignment and Laser Alignment: Tapping Mode and Tapping Mode in Air (soft) should be used for this experiment. Load the experiment to open the Workflow Toolbar, Scan Parameters, List Scan One Channel, and Force Monitor. Access the SETUP in the Workflow Toolbar, and choose other/unknown cantilever. Click the ALIGNMENT STATION icon in the Align window and zoom out as far as possible to see both the laser spot and the tip in the optical field of view. Align the laser to maximize the SUM value on the monitors. Focus on the cantilever by clicking FOCUS UP or FOCUS DOWN. Adjust the illumination for optimal visibility.

Detector Alignment: Utilize two photodetector knobs to align the photodetector so that the red dot is at the center of the Dimension head filter screen. Fine-tune to attain a (0,0) value for vertical and horizontal deflections, respectively.

Focusing on the Sample: Raise the SPM head using the SPM up arrow to ensure sufficient clearance between the tip holder and the sample before rotating the stage. Direct the sample stage so that the laser light shines on the sample. Focus on the surface by moving the SPM head up or down using the SPM up arrow or down arrow.

Verify the parameters by clicking CHECK PARAMETERS and adjust to match the initial scan parameters for Tapping Mode AFM outlined in the Bruker manual in Figure 3.9. Carefully lower the SPM head until the sample surface is focused, being mindful not to crash the head into the sample. Engage the tip by clicking Engage to generate the force vs. distance. Set Channels 1, 2, and 3 to HEIGHT SENSOR, AMPLITUDE ERROR, and PHASE, respectively. Adjust the data scale by clicking the AUTOSCALE icon. Optimize the force during imaging by adjusting the Amplitude Setpoint in Feedback controls. Start by gradually increasing the Setpoint and using the

right arrow, until the blue and red lines significantly differ. Obtain the total adhesion force acting on the particle from the porous substrate, and work of adhesion. Repeat the procedure for different spring constants. Determine which spring constant range is adequate for predicting the adhesive force in this application.

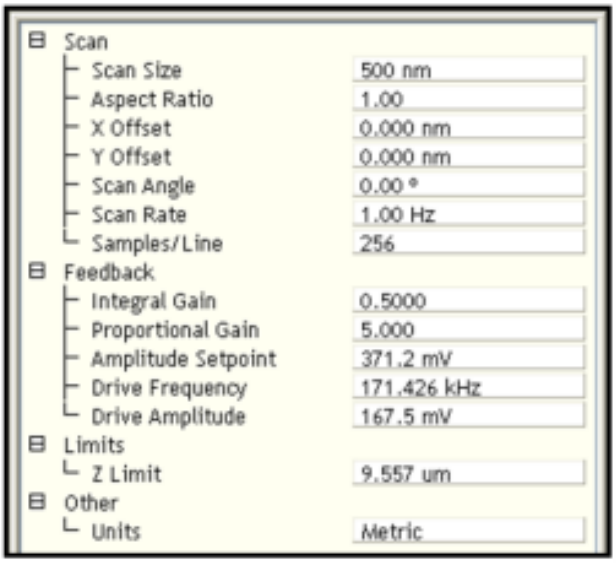

Figure 3.9: Scanning parameters outlined in the Bruker manual.

3.5 Finding critical friction velocity and equilibrium thickness

3.5.1 Critical friction velocity

The particle can be removed when the rolling or sliding criteria are satisfied. Toscano and Ahmadi defined the rolling criteria as a function of impacting angle θ [31]:

$$M_t + F_t\left(\frac{d}{2}\right) + F_l a + F_c\left[-\sin\theta\left(\frac{d}{2}\cos\theta + a\right) + \cos\theta\left(\frac{d}{2}\sin\theta + \frac{d}{2}\right)\right] \geq F_a. \qquad (3.44)$$

The authors transformed the criteria into a set of equations using sublayer flow analysis combined with all the forces mentioned above. The critical shear velocity for rolling motion is as follows:

$$A_1 = \frac{1.07\pi\rho_f d_1^3}{C_c} + \frac{2.9\pi\rho_f d_1^2 C_d}{C_c}\left(\frac{d_1}{2} - \alpha\right) + \frac{0.915\rho_f u^* d_1^3}{\nu}a. \tag{3.45}$$

$$A_2 = \frac{F_c}{u^{*2}}\left[-\sin\theta\left(\frac{d_1}{2}\cos\theta + a\right) + \cos\theta\left(\frac{d_1}{2}\sin\theta + \frac{d_1}{2} - \alpha\right)\right]. \tag{3.46}$$

$$u^* = \left(\frac{F_{po}a}{A_1 + A_2}\right)^{1/2}. \tag{3.47}$$

Toscano and Ahmadi defined the sliding criteria as a function of static friction coefficient μ_s as:

$$F_t + F_c\cos\theta \geq (F_{po} - F_l + F_c\sin\theta)\,\mu_s. \tag{3.48}$$

The critical shear velocity for sliding motion is:

$$u^* = \left[\frac{(F_{po} - \frac{0.915\rho {u^*}^3 {d_1}^3}{\nu} + 1.28E^{*2/5}r^{*1/5}m^{*3/5}V_{cl}^{6/5}sin(\theta)) \times \mu_s}{\frac{2.9\pi\rho_f {d_1}^2 C_d}{C_c} + \frac{1.28E^{*2/5}r^{*1/5}m^{*3/5}}{u^{*2}V_{cl}^{6/5}cos(\theta)}}\right]^{1/2}. \tag{3.49}$$

For each criterion, the critical shear velocity was solved using the bi-section method until the solutions between two consecutive iterations converged within 10^{-10} m/s. The final u^*_{crit} was determined by comparing both criteria and taking the minimum value. The critical shear velocities necessary for sliding detachment are significantly higher than those for rolling detachment. Therefore, the impacting-rolling detachment is the dominant resuspension mechanism of spherical particles in turbulent flows [41].

This section studies critical friction velocity as a function of free-stream velocity and particle diameters. The particle and fluid properties are listed in Table 3.1. Particle diameter ranges from 0.1×10^{-6} to $10\times10^{-6}m$, and free stream velocity ranges from 0.1, 0.5, 1.0, 1.5 to 2 m/s.

Table 3.1: Particle and Fluid Properties for critical friction velocity study.

Fluid	**Value**
Particle density ρ_p	2,260 kg/m^3
Particle diameter d_p	0.1×10^{-6} to 10×10^{-6} m
Fluid density ρ_f	1.225 kg/m^3
Fluid viscosity μ_f	1.7894×10^{-5} kg/ms
Temperature	302 K
Free stream velocity	0.1 to 2 m/s

Figure 3.10 shows how critical friction velocity behaves with varying free-stream velocity and particle diameters. For a constant free stream velocity, the critical friction velocity decreases with an increase in particle diameter. Smaller particles are harder to be removed by the fluid and free stream particles because hydrodynamic torque, drag force, lift force, and impact force are proportional to the particle's diameter, as expressed in Equations 3.23, 3.25, 3.28 and 3.29. The fluid at the sublayer flow must have larger momentum to induce sufficient forces to remove smaller particles. For a fixed particle diameter, the critical friction velocity decreases as the free stream velocity increases. As free stream particles carry more momentum at higher free stream velocity, the impact force acting on adhered particles is larger. Therefore, the adhered particle is easier to remove, hence, lower critical shear velocity. However, free stream particles do not carry much momentum at lower free stream velocity, the impact force acting on adhered particles is smaller; therefore, the adhered particle has to rely on the drag force and lift force exerted by the fluid to be removed, hence, higher critical shear velocity.

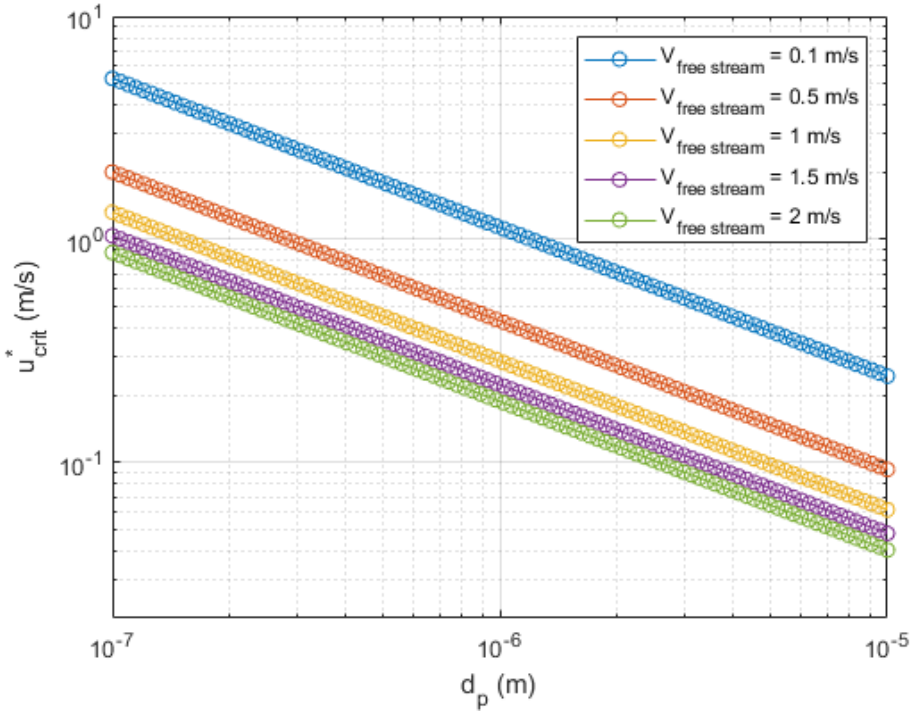

Figure 3.10: Critical friction velocity u^*_{crit} as a function of particle diameter and free stream velocity $V_{freestream}$.

3.5.2 Equilibrium thickness - Analytical result

Based on the above analysis, the ultimate goal of the model is to estimate for δ_c from the hydraulic diameter at equilibrium where the friction velocity is equal to u^*_{crit}. Analytically estimating friction velocity on a smooth wall, as suggested by Chavez et al. [29]:

$$u^* = \sqrt{\frac{f}{2}} V_{freestream}. \tag{3.50}$$

where f is friction coefficient given by:

$$f = \frac{0.316}{4Re^{1/4}}. \tag{3.51}$$

Under the above assumptions, the equation can be expressed in terms of the channel radius h as:

$$u^*_{crit} = \sqrt{\frac{0.316}{8(\frac{V_{freestream}2h_{og}}{\nu_f})^{0.25}}} V_{freestream}. \tag{3.52}$$

Using conservation of mass to predict the mean velocity when the new channel radius h_{new} is at equilibrium, with h_{og} is the channel radius when there is no particle deposited, yields:

$$V_{inlet}h_{og} = V_{freestream}h_{new}. \tag{3.53}$$

where

$$V_{freestream} = \frac{V_{inlet}h_{og}}{h_{new}}. \tag{3.54}$$

Using Equation 3.52 and 3.53, h_{new} is solved, and the particle diffusion thickness at equilibrium $\delta_c = h_{og} - h_{new}$. Because critical shear velocity u^*_{crit} is a function of mean flow velocity $V_{freestream}$, it is necessary to use $V_{freestream}$ calculated in this step and iterate until the parameter between two consecutive iterations converge within 10^{-10} m/s.

3.5.3 Numerical Validation

3.5.3.1 Configuration, set-up, computational domain

Particle and working fluid properties are listed in Table 3.2. Two-dimensional numerical simulation for channel flow is performed in ANSYS Fluent. Air at different inlet velocities goes through a channel with an original hydraulic diameter of 4 inches. The inlet velocity is varried at 0.6, 0.7, 0.8, 0.9, 1.0, and 1.08 m/s, respectively, corresponding for Re of 4,173; 4,869; 5,564; 6,260; 5,955; and 7,512. The hydraulic diameter will change at different deposition thicknesses. Shear stress, which is then used to calculate the the friction velocity from Equation 3.50, is measured at a hydraulic distance where the flow is fully developed. The flow is assumed to be turbulent and fully developed before and after reaching asymptotic deposition. The set-up and computational domain are described in Figure 3.11.

Table 3.2: Particle and Fluid Properties for equilibrium thickness study.

Fluid	Value
Particle density ρ_p	2,260 kg/m^3
Particle diameter d_p	7.5×10^{-6} m
Fluid density ρ_f	1.225 kg/m^3
Fluid viscosity μ_f	1.7894×10^{-5} kg/ms
Temperature	302 K
Inlet velocity	0.6 to 1.08 m/s
Original hydraulic diameter	4 inches

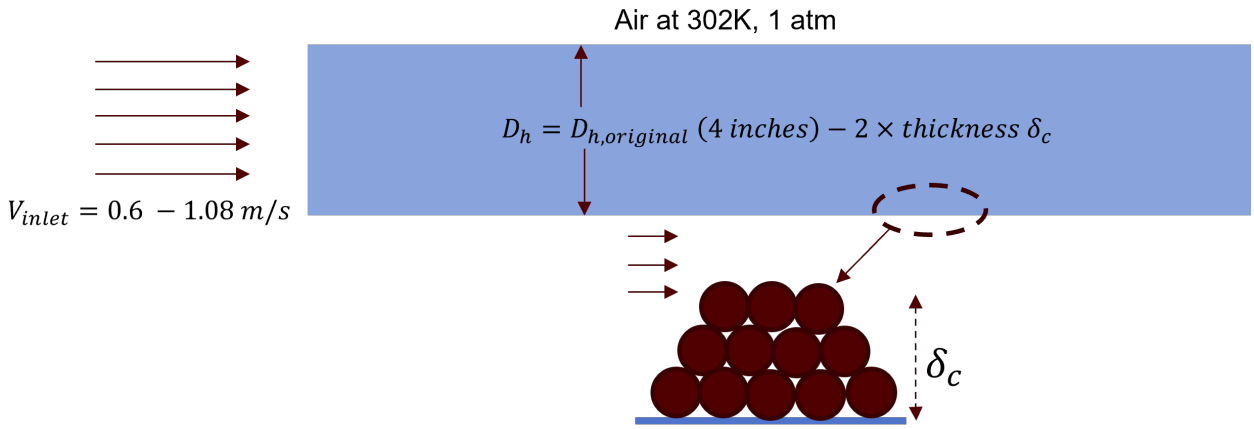

Figure 3.11: Flow configuration and computational domain.

3.5.3.2 Grid convergence study

A grid convergence study is conducted at an inlet velocity of 1.08 m/s, and the parameter of interest is shear stress at a fully developed flow location. k-ϵ realizable turbulence model is utilized for the study. The turbulence model has been widely used for shear stress prediction in computational fluid dynamics (CFD) simulations. It is considered a good, reliable, and widely accepted model for simulating turbulent flows. The k-ϵ model can capture the essential features of

turbulence and predict the turbulence intensity and length scale, which are important for calculating turbulence shear stress.

Table 3.3 and Figure 3.12 shows how the fully developed shear stress changes as the number of mesh element increases. The parameter of interest starts approaching an asymptotic value at 227,095 elements. At 300,578 elements, the parameter of interest does not change significantly. Maximum y^+ is 0.15529, minimum y^+ is 0.02369, and average y^+ is 0.02717. Therefore, it is concluded that the mesh has converged at 227,095 elements to save computational time. This mesh is then used to run at different inlet velocities.

Table 3.3: Number of mesh elements and shear stress τ_s.

Number of mesh elements	**Shear stress τ_s (Pa)**
95,807	0.005523
158,604	0.0059
227,095	0.006141
300,578	0.006147

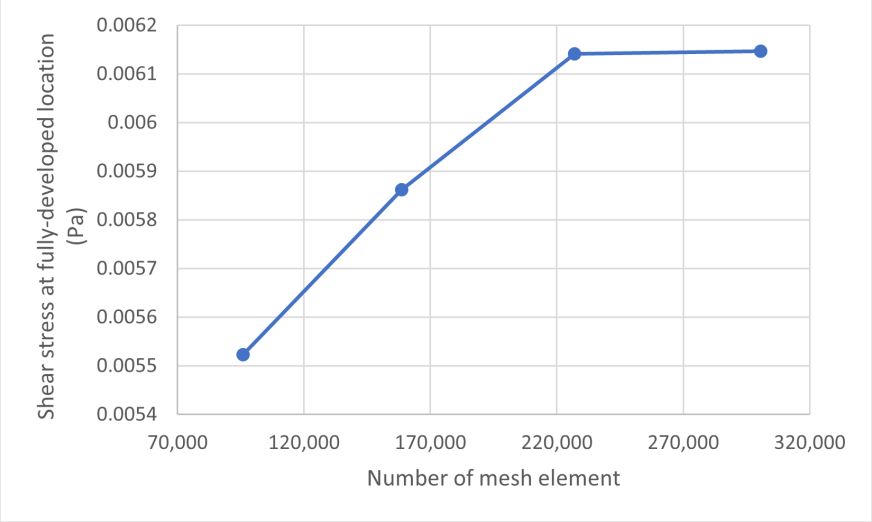

Figure 3.12: The grid convergence study is conducted at an inlet velocity of 1.08 m/s.

3.5.3.3 Results and discussion

Critical shear velocity for graphite particles with a diameter of 7.5 μm and density of 2,260 kg/m^3 is calculated using Equations 3.47 and 3.49 and taking the minimum value. Equations 3.50 to 3.54 are iteratively solved to determine the asymptotic deposition thickness δ_c. It is important to note that the critical shear velocity decreases due to the decreasing hydraulic diameter as the free stream velocity increases. As free stream particles carry more momentum at higher free stream velocity, the impact force acting on adhered particles is larger. Therefore, the adhered particle is easier to remove, hence, lower critical shear velocity. In Table 3.4, the asymptotic deposition thickness δ_c is estimated for an inlet velocity of 0.6, 0.7, 0.8, 0.9, 1.0, and 1.08 m/s and its respective u^*_{crit}. Fluid shear stress where the flow is fully developed is calculated with the converged grid using ANSYS Fluent. The CFD result is then used to estimate the shear velocity with Equation 3.50. The difference between analytical u^*_{crit} and shear velocity u^* generated by CFD is then presented. The maximum difference between u^*_{crit} calculated using the proposed iteration scheme and u^* generated by CFD is 8.23%, whereas the minimum difference is 0.22%. It is concluded that the suggested methodology in this study is adequate to predict the critical shear velocity and equilibrium deposition thickness δ_c.

Table 3.4: Comparison between analytical u^*_{crit} and shear velocity u^* generated by CFD.

Inlet velocity (m/s)	δ_c **(m)**	u^*_{crit} **(m/s) Analytical**	**Shear stress (Pa) CFD**	u^* **(m/s) CFD**	**Difference %**
0.6	0.0214	0.07262	0.00767105	0.079133	8.23
0.7	0.0169	0.07210	0.00713851	0.076337	5.55
0.8	0.0124	0.07165	0.00679733	0.074491	3.81
0.9	0.008	0.07126	0.00649491	0.072815	2.13
1.0	0.0037	0.07091	0.00625974	0.071484	0.8
1.08	0.000217	0.07065	0.00614101	0.070803	0.22

3.6 Nondimensionalization and Scaling Analysis

Starting from the final expression where mass is deposited as a function of time in exponential form:

$$m(t) = m_{eq}(1 - e^{-\frac{3t}{2t_{sat}}}) = \delta_c A(1 - \epsilon_{3D})\rho_{part}(1 - e^{-\frac{3t}{2t_{sat}}}). \tag{3.55}$$

with

$$t_{sat} = \frac{15m_{eq}}{16J_m A} = \frac{15\delta_c(1 - \epsilon_{3D})\rho_p}{16m_p u_d^+ u^* C_0}. \tag{3.56}$$

The Stokes number is defined as:

$$Stk = \frac{\tau U}{L_c}. \tag{3.57}$$

where U is free-stream velocity, L_c is characteristic length (which is hydraulic diameter D_h in this study) and τ is particle relaxation time expressed as:

$$\tau = \frac{\rho_p d_p^2}{18\mu_f}. \tag{3.58}$$

Nondimensionalizing t_{sat} can be peformed by dividing the parameter by the characteristic time of the flow L_c/U and expressing in terms of Stk, which yields:

$$\frac{t_{sat}}{L_c/U} = \frac{\frac{15\delta_c(1-\epsilon_{3D})\rho_p}{16m_p u_d^+ u^* C_0}}{\tau}\frac{\tau U}{L_c}. \tag{3.59}$$

$$\frac{t_{sat}U}{L_c} = \frac{\frac{15\delta_c(1-\epsilon_{3D})\rho_p}{16m_p u_d^+ u^* C_0}}{\frac{\rho_p d_p^2}{18\mu_f}}Stk. \tag{3.60}$$

Defining t_{sat}^+ as a non-dimensional saturation time $t_{sat}U/L_c$, and algebraically simplifying the expression:

$$t_{sat}^+ = \frac{135}{8}\frac{1 - \epsilon_{3D}}{u_d^+}\frac{\delta_c}{d_p}\frac{\nu_f}{d_p u^*}Stk\frac{\rho_f}{C_0 m_p}. \tag{3.61}$$

$$t_{sat}^+ = \frac{135}{8}\frac{1 - \epsilon_{3D}}{u_d^+}\frac{\delta_c}{d_p}\frac{1}{Re_p}Stk\frac{\rho_f}{C_0 m_p}. \tag{3.62}$$

The last term $\frac{\rho_f}{C_0 m_p}$ depicts the effect of particle concentration on the non-dimensional saturation time t^+_{sat}. Expanding the mass of each particle as a product between the volume of each particle and particle density, it becomes the mass ratio of total fluid mass and total particle mass as follows:

$$\frac{\rho_f}{C_0 m_p} = \frac{\rho_f}{\rho_p}\frac{1}{C_0 V_p} = \frac{\rho_f}{\rho_p}\frac{\Sigma V_f}{\Sigma V_p} = \frac{\Sigma m_f}{\Sigma m_p}. \tag{3.63}$$

A complete non-dimensional saturation time t^+_{sat} becomes:

$$t^+_{sat} = \frac{t_{sat} U}{L_c} = \frac{135}{8}\left(\frac{1-\epsilon_{3D}}{u^+_d}\right)\left(\frac{\delta_c}{d_p}\right)\left(\frac{1}{Re_p}\right)\left(\frac{\Sigma m_f}{\Sigma m_p}\right)(Stk). \tag{3.64}$$

The friction velocity u^* was estimated using friction factor f computed from the Blasius correlation corrected for non-circular ducts by replacing diameter with the equivalent diameter:

$$u^* = \sqrt{\frac{f}{2}}U \tag{3.65}$$

$$f = \frac{0.316}{4Re^{0.25}} \tag{3.66}$$

Assuming that the flow is fully developed and steady, Stk is dependent on non-dimensional particle relaxation time τ^+ and Re and can be expressed as follows:

$$\tau^+ = \frac{d_p^2 u^* 2\rho_p}{18\nu_f^2 \rho_f} = \frac{\rho_p d_p^2 U}{18\mu_f D_h}\frac{u^{*2}\rho_f}{\mu_f}\frac{D_h}{U} = Stk\frac{\frac{f}{2}U^2\rho_f}{\mu_f}\frac{D_h}{U} = Stk\frac{f}{2}\frac{U\rho_f D_h}{\mu_f} = Stk\frac{f}{2}Re. \tag{3.67}$$

$$Stk = \frac{\tau^+}{\frac{f}{2}Re} \tag{3.68}$$

The non-dimensional saturation time t^+_{sat} has been expressed in terms of related non-dimensional numbers. The scaling analysis requires that each involved non-dimensional number needs to be scaled; hence, the scaling law is given by:

$$(u^+_d)_M = (u^+_d)_P. \tag{3.69}$$

$$(Re_p)_M = (Re_p)_P \leftrightarrow \left(\frac{d_p u^*}{\nu_f}\right)_M = \left(\frac{d_p u^*}{\nu_f}\right)_P. \tag{3.70}$$

$$\left(\frac{\delta_c}{d_p}\right)_M = \left(\frac{\delta_c}{d_p}\right)_P. \tag{3.71}$$

$$(Re)_M = (Re)_P \leftrightarrow \left(\frac{\rho_f U D_h}{\mu_f}\right)_M = \left(\frac{\rho_f U D_h}{\mu_f}\right)_P. \tag{3.72}$$

$$\left(\frac{\Sigma m_f}{\Sigma m_p}\right)_M = \left(\frac{\Sigma m_f}{\Sigma m_p}\right)_P \leftrightarrow \left(\frac{\rho_f}{C_0 m_p}\right)_M = \left(\frac{\rho_f}{C_0 m_p}\right)_P. \tag{3.73}$$

To have 3.69 valid, three non-dimensional terms of the particle velocity needs to be scaled:

$$(Sc)_M = (Sc)_P \leftrightarrow \left(\frac{\nu_f}{\frac{kT}{3\pi\mu_f d_p}}\right)_M = \left(\frac{\nu_f}{\frac{kT}{3\pi\mu_f d_p}}\right)_P. \tag{3.74}$$

$$(\tau^+)_M = (\tau^+)_P \leftrightarrow \left(\frac{d_p^2 u^* \rho_p}{18\nu_f \rho_f}\right)_M = \left(\frac{d_p^2 u^* \rho_p}{18\nu_f \rho_f}\right)_P. \tag{3.75}$$

$$(g^+)_M = (g^+)_P \leftrightarrow \left(\frac{\nu_f g}{u^*}\right)_M = \left(\frac{\nu_f g}{u^*}\right)_P. \tag{3.76}$$

3.7 Parametric Study

There are nine (9) parameters that need consideration when performing scaling analysis and parametric study: fluid viscosity μ_f, fluid density ρ_f, temperature T, particle diameter d_p, particle density ρ_p, freestream velocity U, deposition geometry D_h, friction velocity u^* and particle concentration C_0. There are also six (6) equations relating these parameters to the non-dimensional numbers, including Eqs. 3.65, 3.70, 3.72, 3.73, 3.74, and 3.75. Keeping fluid's properties constant (μ_f and ρ_f) at fixed temperature T, and varying one non-dimensional number while keeping the others constant can be made by changing in different parameters, which can be expressed as a calculating sequence below:

$$Sc = \frac{\nu_f}{\frac{kT}{3\pi\mu_f d_p}} \rightarrow d_p = \frac{SckT}{3\pi\mu_f\nu_f}. \tag{3.77}$$

$$Re_p = \frac{d_p u^*}{\nu_f} \rightarrow u^* = \frac{Re_p \nu_f}{d_p}. \tag{3.78}$$

$$u^* = \sqrt{\frac{f}{2}}U \rightarrow U = \frac{u^*}{\sqrt{\frac{f}{2}}}. \tag{3.79}$$

$$Re = \frac{D_h U}{\nu_f} \rightarrow D_h = \frac{Re\nu_f}{U}. \tag{3.80}$$

$$\tau^+ = \frac{d_p^2 u^{*2} \rho_p}{18\nu_f^2 \rho_f} \rightarrow \rho_p = \frac{\tau^+ 18\nu_f^2 \rho_f}{d_p^2 u^{*2}}. \tag{3.81}$$

$$\frac{\Sigma m_f}{\Sigma m_p} = \frac{\rho_f}{C_0 m_p} \rightarrow C_0 = \frac{\rho_f}{\frac{\Sigma m_f}{\Sigma m_p}\frac{4}{3}\pi\frac{d_p^3}{8}\rho_p}. \tag{3.82}$$

Gravitational sedimentation term is defined as $g^+ = \frac{\nu_f g}{u^*}$. While the fluid kinematic viscosity ν_f and gravitation acceleration g is constant, the only parameter that can alter g^+ is the friction velocity u^*. According to the calculation sequence above with known fluid properties, g^+ can be kept constant by not varying Sc and Re_p. Additionally, Stk is dependent on non-dimensional particle relaxation time τ^+ and Re as expressed in Equation 3.68. Hence, a parametric study can be done by studying how t_{sat}^+ and u_d^+ changes by varying τ^+, Re, and mass ratio $\frac{\Sigma m_f}{\Sigma m_p}$.

A parametric study was conducted by choosing air as the working fluid at 302 K. The non-dimensional particle relaxation time τ^+ is varied from 0.04 to 4.6, and Re is varied from 4,173 to 7,512. Using the above-mentioned calculation sequence, the particle diameter remained constant while the particle density varied from 900 kg/m^3 to 11,300 kg/m^3. The mass ratio of the fluid to particles per unit volume ranges from 0.45 to 4.5×10^8, and the particle concentration is calculated accordingly, ranging from 5.45×10^3 $particles/m^3$ to 5.45×10^{12} $particles/m^3$. The new inlet velocity and new hydraulic diameter are calculated for each Re, ranging from 0.6 m/s to 1.08 m/s and from 4 to 30 $inches$, respectively.

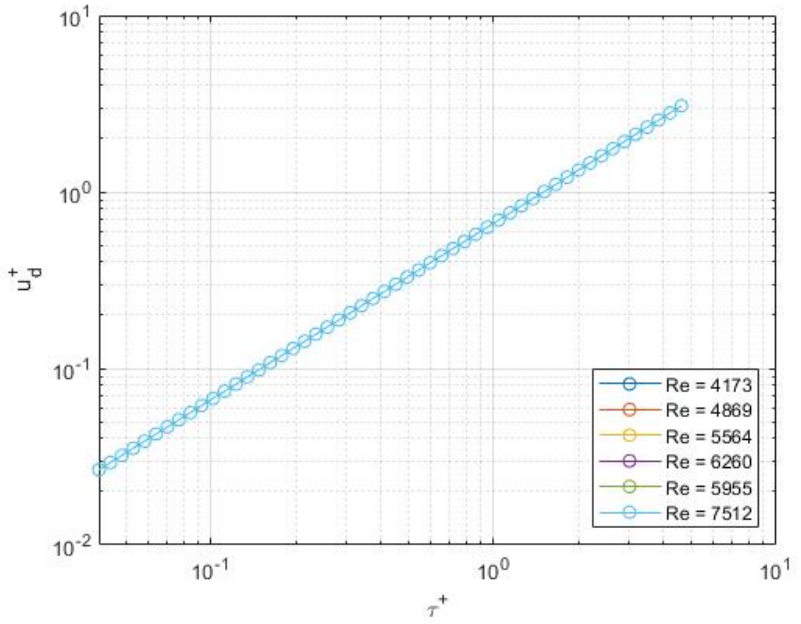

Figure 3.13: Non-dimensional deposition velocity u_d^+ vs. non-dimensional particle relaxation time τ^+ at different Re.

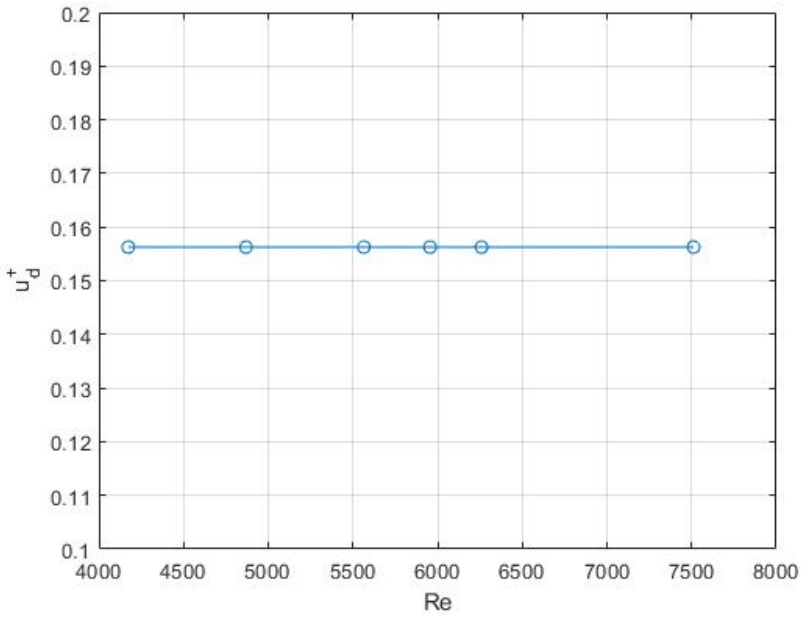

Figure 3.14: Non-dimensional deposition velocity u_d^+ vs. Re.

Figure 3.13 shows the variation of non-dimensional deposition velocity as a function of particle relaxation time. For a fixed Re, the non-dimensional particle deposition velocity increases with an increase in non-dimensional relaxation time. At higher values of τ^+, the particles take a longer time to adjust themselves back to the fluid streamlines, resulting in a higher probability of being deposited on the wall. Hence, the non-dimensional deposition velocity increases with an increase in non-dimensional particle relaxation time. Figure 3.14 shows the variation of non-dimensional deposition velocity with Reynolds number (Re). The non-dimensional deposition velocity remains constant as Re increases due to increasing free-stream velocity and hydraulic diameter while maintaining a constant non-dimensional particle relaxation time because Re does not directly affect Brownian diffusion (Sc), eddy-impaction (τ^+), and gravitational sedimentation (g^+).

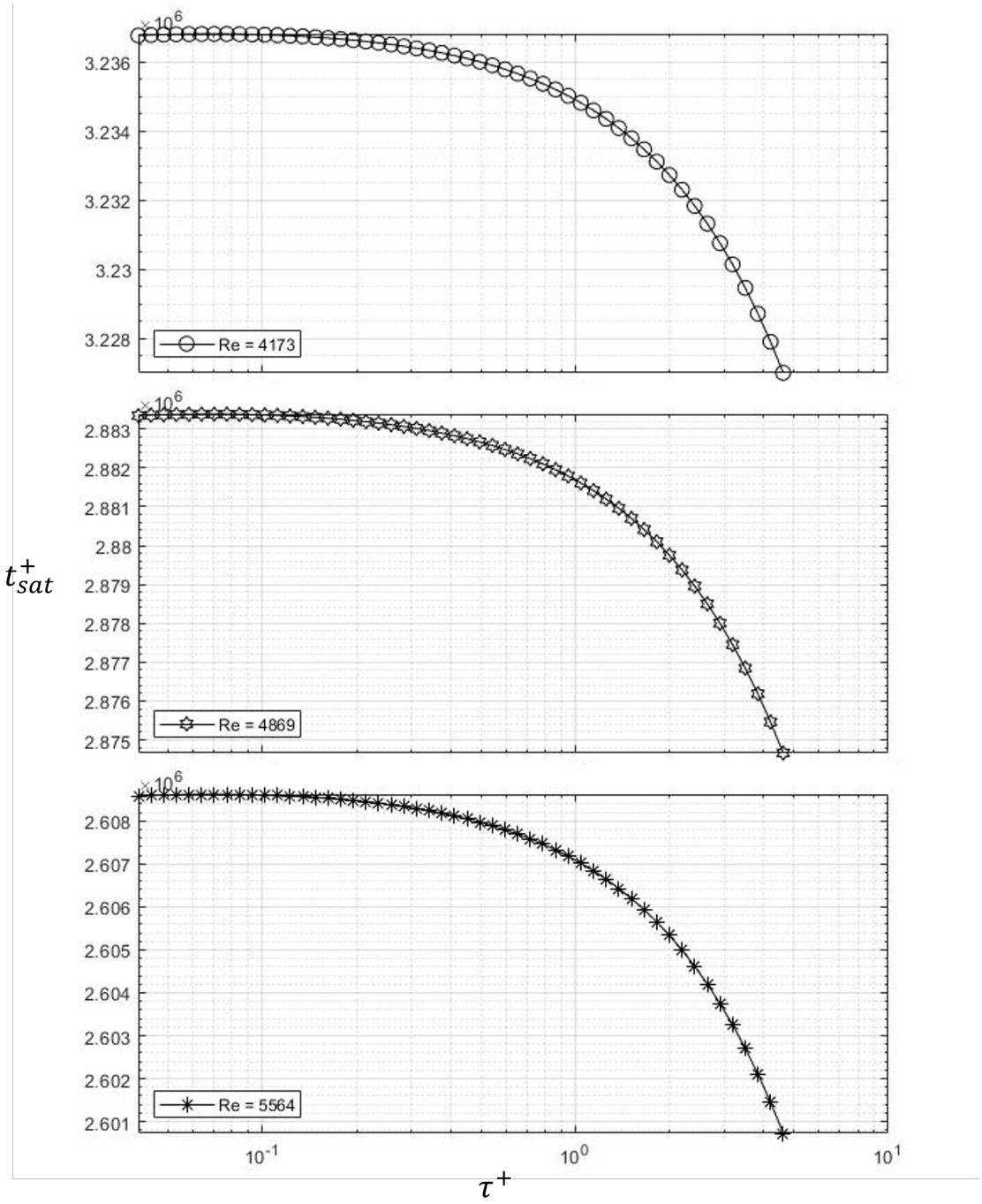

Figure 3.15: Non-dimensional saturation time t_{sat}^{+} vs. particle relaxation time τ^{+} at different Re = 4,173; 4,869; and 5,564.

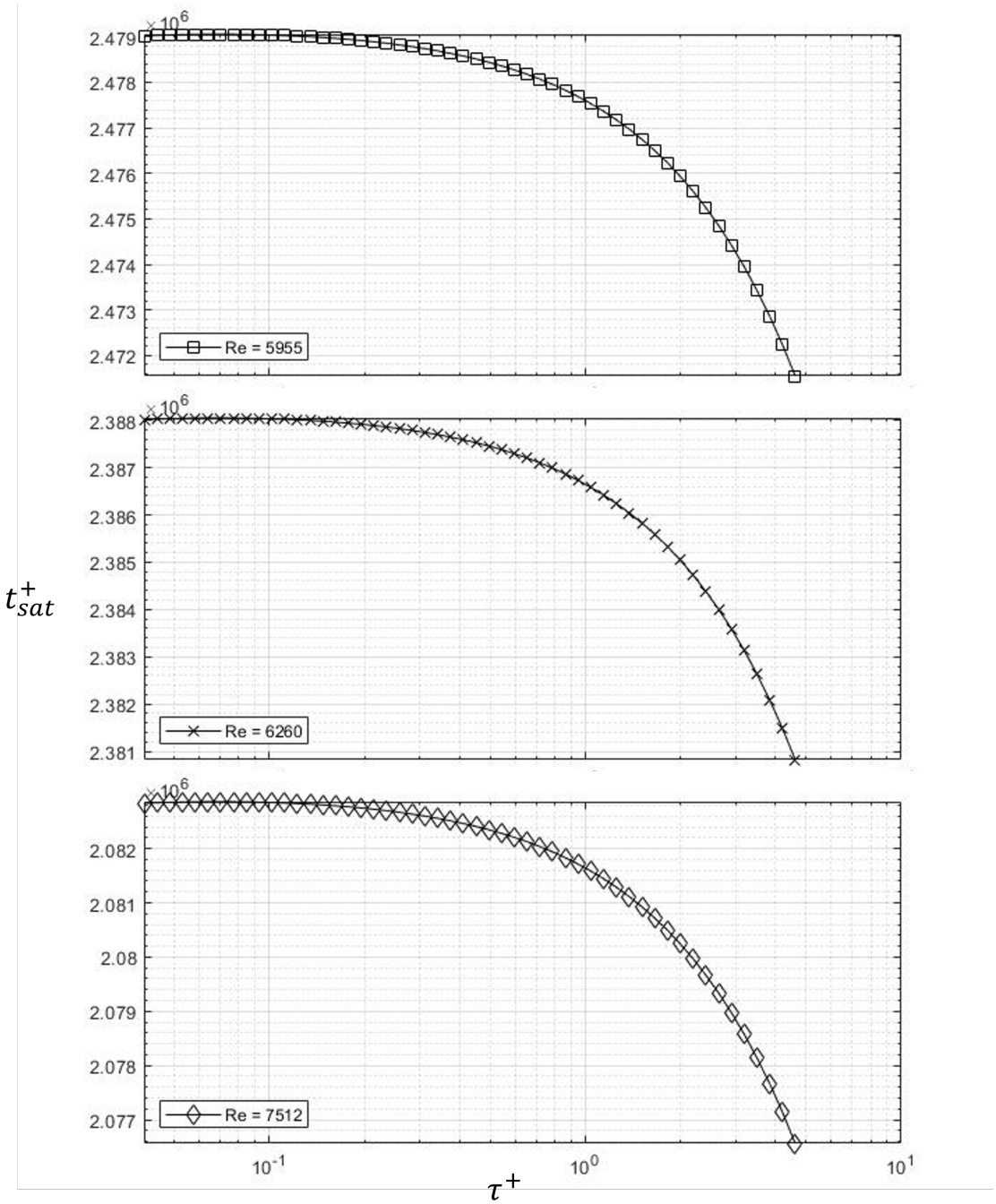

Figure 3.16: Non-dimensional saturation time t^+_{sat} vs. particle relaxation time τ^+ at different Re = 5,955; 6,260; and 7,512.

As the particle relaxation time increases for a fixed Re, the deposition velocity increases, as shown in Figure 3.13, resulting in more particles being deposited over a unit area and time. In

general, as more particles are deposited, the surface takes less time to become saturated and approach equilibrium faster. Therefore, the saturation and equilibrium time decrease with increase in non-dimensional particle relaxation time, as shown in Figures 3.15 and 3.16. For a fixed particle relaxation time (τ^+) both saturation and equilibrium times decrease with an increase in Re. At higher value of Re, the property of particles flow through the channel without getting deposited to the wall. Since Stk can be expressed as a function of τ^+ and Re in Equation 3.68 for fully developed flow, the complete non-dimensional saturation time t^+_{sat} from Equation 3.64 can also be written as:

$$t^+_{sat} = \frac{t_{sat}U}{L_c} = \frac{135}{8}\left(\frac{1-\epsilon_{3D}}{u^+_d}\right)\left(\frac{\delta_c}{d_p}\right)\left(\frac{1}{Re_p}\right)\left(\frac{\Sigma m_f}{\Sigma m_p}\right)\frac{\tau^+}{\frac{f}{2}Re} \tag{3.83}$$

Express Equation 3.83 so that it is a clear function of τ^+:

$$t^+_{sat} = \frac{t_{sat}U}{L_c} = \frac{135}{8}\left(\frac{1-\epsilon_{3D}}{\frac{f}{2}Re}\right)\left(\frac{\delta_c}{d_p}\right)\left(\frac{1}{Re_p}\right)\left(\frac{\Sigma m_f}{\Sigma m_p}\right)\frac{\tau^+}{u^+_d} \tag{3.84}$$

$$t^+_{sat} = \frac{t_{sat}U}{L_c} = \frac{135}{8}\left(\frac{1-\epsilon_{3D}}{\frac{f}{2}Re}\right)\left(\frac{\delta_c}{d_p}\right)\left(\frac{1}{Re_p}\right)\left(\frac{\Sigma m_f}{\Sigma m_p}\right)\frac{\tau^+}{0.057Sc^{-2/3} + 4.5\times10^{-4}\tau^{+2} + \tau^+ g^+} \tag{3.85}$$

Non-dimensional particle relaxation time appears in both the numerator and denominator of Equation 3.85, which will make t^+_{sat} slightly increase as τ^+ increases and reach a critical value before decreasing, as shown in Figure 3.17. Less than this critical value (Stk is very small, and particles follow well the fluid streamlines), the deposition velocity is mainly governed by Brownian diffusion (Sc), which is the characteristic random wiggling motion of small airborne particles in the air. The diffused particles into the wall are easily accelerated by the swirls motion of the turbulent sublayer flow, causing non-dimensional time t^+_{sat} to decrease. As Stk decreases, t^+_{sat} slightly decreases in the Brownian diffusion-dominated region. Taking the derivative of the Equation 3.85 with respect to τ^+ and setting it to zero, one can determine the critical non-dimensional relaxation time τ^+_{crit} as:

$$\tau^+_{crit} = \sqrt{\frac{0.057}{4.5\times10^{-4}}}Sc^{-1/3} \tag{3.86}$$

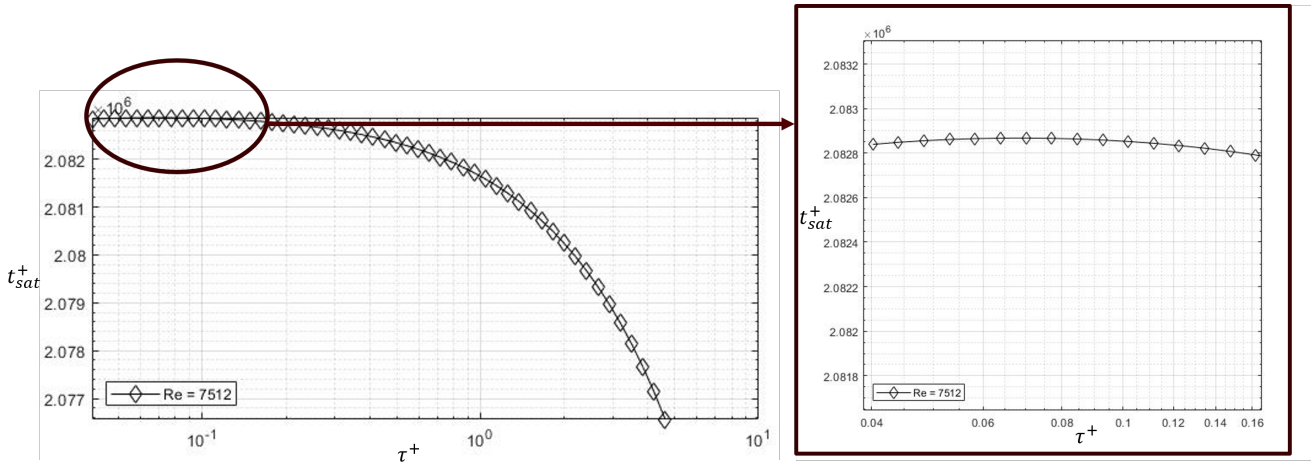

Figure 3.17: t^+_{sat} slightly increases as τ^+ increases and reaches a critical value before decreasing.

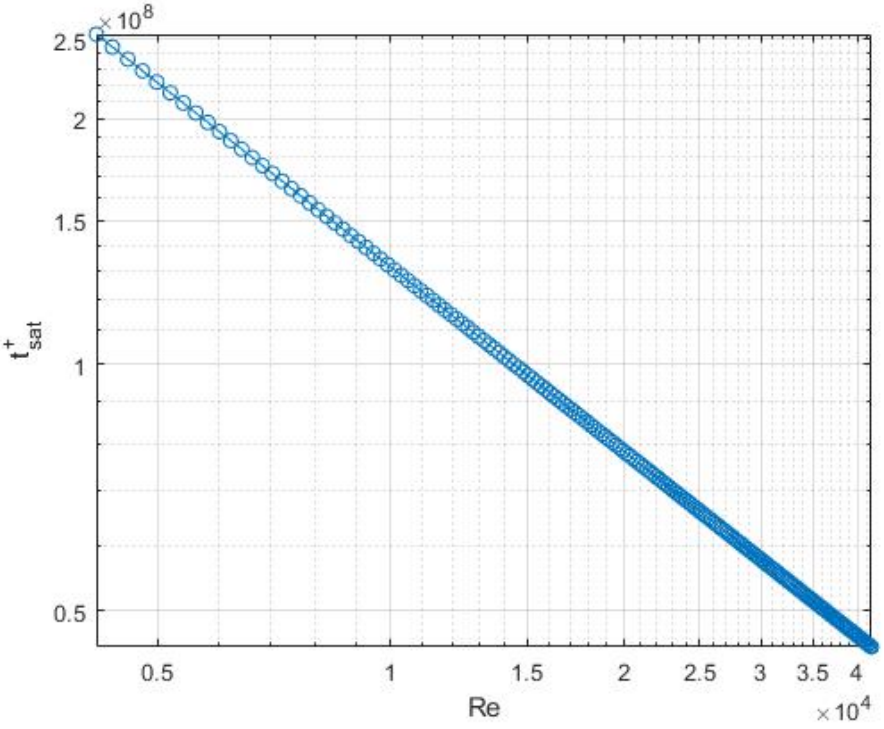

Figure 3.18: Non-dimensional saturation time t^+_{sat} vs. Re.

The non-dimensional particle deposition velocity remains constant for a constant non-dimensional

particle relaxation time and an increasing Re due to increasing free-stream velocity and/or hydraulic diameter. For larger free-stream velocity and hydraulic diameter, the characteristic time of the flow increases, leading to a decrease in non-dimensional saturation time as depicted in Figure 3.18. However, the actual dimensional time remains constant because the parameter is independent of the flow characteristic time, as shown in Equation. 3.56.

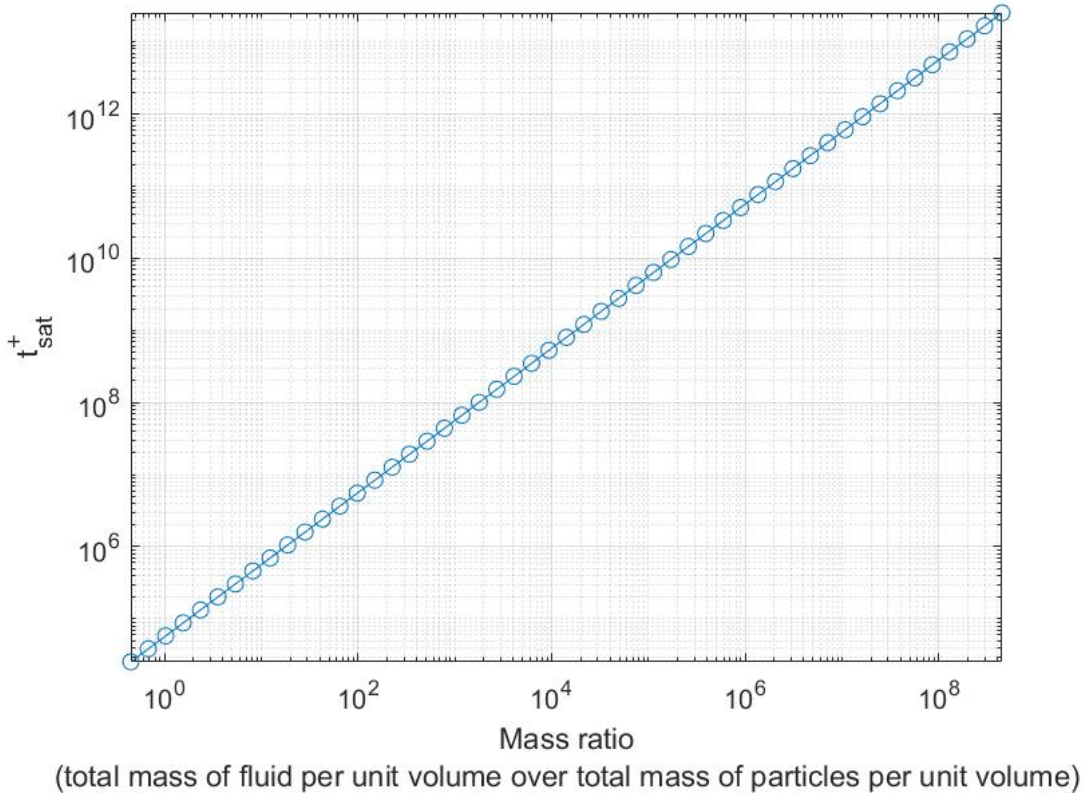

Figure 3.19: Non-dimensional saturation time t^+_{sat} vs. Mass ratio.

For a constant Re and non-dimensional particle relaxation time, the mass ratio of fluid and particles per unit volume increases, which means fewer particles being presented per unit volume, and fewer particles being deposited on the wall. As deposition velocity decreases, the time required to reach saturation increases. Figure 3.19 shows that the non-dimensional saturation time decreases as the mass ratio decreases, i.e., particle concentration increases.

Preliminary calculations to predict the asymptotic deposition behavior in a low temperature and low pressure condition are conducted with air at 302K as the working fluid. The inlet velocity values were varied. The inlet velocity values of 0.6, 0.7, 0.8, 0.9, 1.0, and 1.08 m/s, correspond to Re of 4,173; 4,869; 5,564; 6,260; 5,955; and 7,512, respectively. The hydraulic diameter is 0.1016 m (or 4 inches), deposited particles are graphite dust with a diameter of 7.5 μm and density of 2,260 kg/m^3, and particle concentration at 3.27×10^{10} $particles/m^3$. The total adhesion force is approximated at 4,590.6 nN.

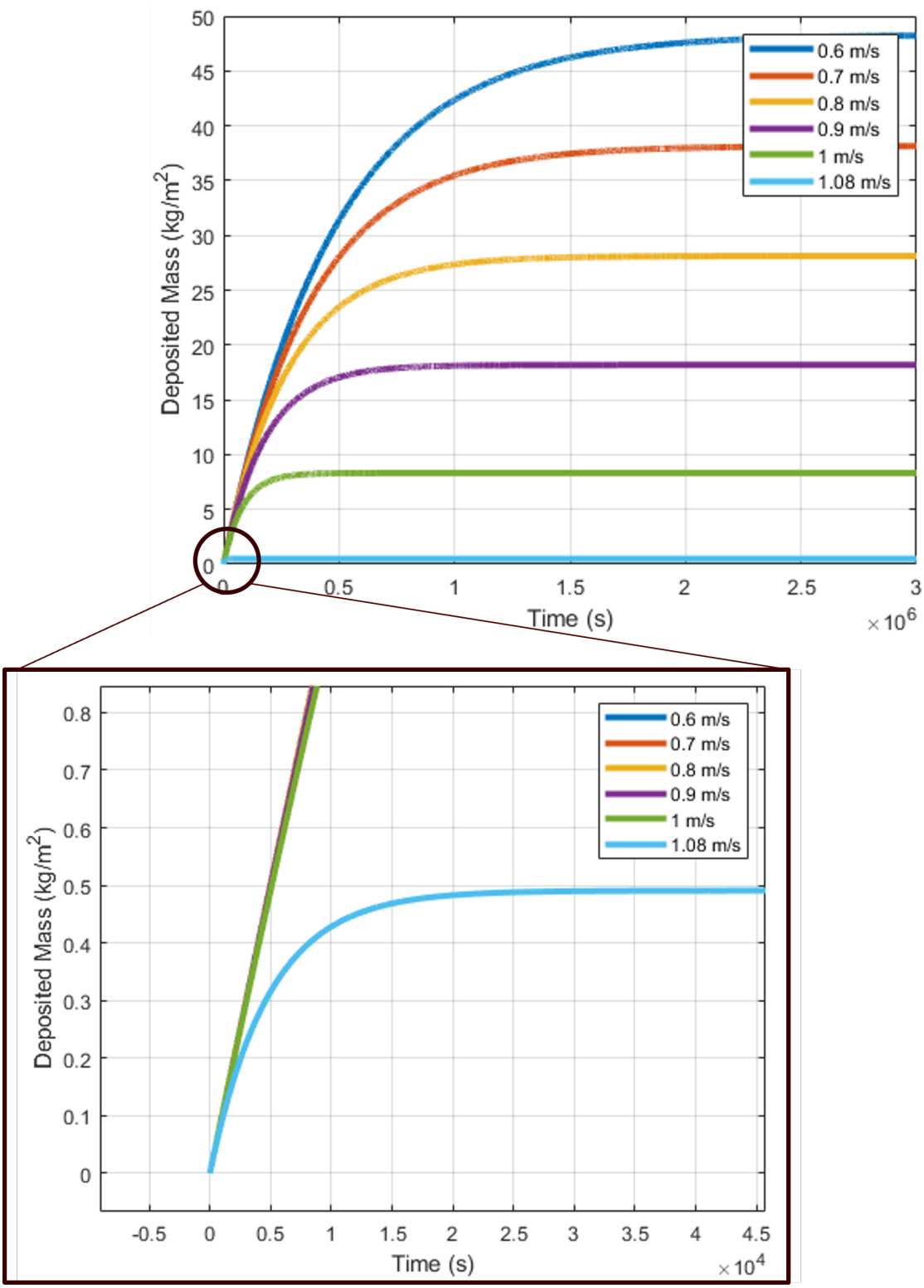

Figure 3.20: Asymptotic deposition behavior predicted in this study.

Table 3.5: Saturation time and equilibrium time for different inlet velocity.

Inlet velocity (m/s)	**Saturation time (s)**	**Saturation time (hrs)**	**Equilibrium time (s)**	**Equilibrium time (hrs)**
0.6	7.17E+05	199.05	2.20E+06	610.50
0.7	5.66E+05	157.22	1.74E+06	482.19
0.8	4.17E+05	115.85	1.28E+06	355.31
0.9	2.70E+05	74.88	8.27E+05	229.67
1.0	1.23E+05	34.28	3.78E+05	105.13
1.08	7.28E+03	2.02	2.23E+04	6.20

The asymptotic deposition behavior for different inlet velocities is presented in Figure 3.20 and the predicted saturation and equilibrium times are listed in Table 3.5. As the inlet velocity increases, the saturation and equilibrium time decreases for the same particle concentration. When the inlet velocity exceeds 1.08 m/s, no deposition occurs because the critical friction velocity of the 7.5 μm graphite particle is less than the shear velocity of the fluid, and the predicted thickness is negative. There is an abrupt decrease in saturation and equilibrium time when increasing the inlet velocity from 1.0 m/s to 1.08 m/s, from 34.28 hours to 2.02 hours, and from 105.13 hours to 6.2 hours. It is recommended to perform validation experiments in this velocity regime as it yields a more reasonable run time. The predicted asymptotic mass deposited per unit area at 0.6, 0.7, 0.8, 0.9, 1.0, and 1.08 m/s inlet velocity is 48.31, 38.16, 28.2, 18.18, 8.32, and 0.49 kg/m^2. As the inlet velocity increases, asymptotic deposited mass decreases for the same particle concentration. It is easier to remove particles because the critical shear velocity is smaller for larger free stream velocities, with fewer particles being deposited; hence, smaller deposition mass.

4. SUMMARY

“Plate-out" refers to the deposition or buildup of solid material on a surface, which can have consequences such as increasing the risk of criticality or corrosion and can also affect the efficiency of equipment and systems. Current plate-out codes predicting fission products and graphite dust transport are only accessible for internal institutional use only apply to the nuclear application even though porous particle deposition is crucial to many industrial heat recovery systems. The numerical findings based on the original geometry may be imprecise due to the accumulating deposition. The objective of this study is to develop a mathematical model for particle deposition under a fully-developed, turbulent channel flow condition, taking the effect of the change in geometry over time.

Wood’s model (1981) for empirically estimating the non-dimensional particle deposition rates in turbulent flows is governed by 3 phenomena: Brownian diffusion, eddy-impaction, and gravitational sedimentation. Particle and mass flux to the wall are derived. The deposition is termed undersaturated when the removal rate is negligible compared to the deposition rate. The deposited mass increases linearly with time in the undersaturated region. The deposition is termed saturated when the removal rate becomes considerable compared to the deposition rate. The particles start building up in layers. The transition time between undersaturated and saturated conditions is defined as saturation time. Equilibrium is determined when deposition and removal rates are equal. Thickness grows exponentially and reaches an asymptotic value in the form of an exponential function according to the asymptotic deposition model. The mass deposited as a function of time can be expressed as a function of equilibrium thickness, unit area, porosity, and particle density, as expressed in Equation 3.20. Saturation time can be expressed as a function of equilibrium thickness, particle properties, deposition velocity, friction velocity, and particle concentration, as expressed in Equation 3.18.

The particle removal mechanism is examined by analyzing all forces acting on the particle, including, hydrodynamic torque, impact force, lift force, drag force, and four (4) adhesion forces.

Atomic Force Microscope (AFM) measurement is determined to be an adequate methodology to measure the total adhesion force. An experimental procedure with Bruker's Dimension AFM-ICON has been proposed. The porous substrate can be obtained by placing a thin 5mm x 5mm film at the location where the flow is fully developed. The thin film should not be too thick (above 0.5mm) as the thickness will easily alter the flow properties, leading to inaccurate deposition data. Particle concentration is set to $3.27 \times 10^{10}\ particles/m^3$, corresponding to a particle injection mass flow rate of 0.000152 kg/s for graphite properties with a hydraulic diameter of 4 inches. Inlet velocity is recommended to be set at 1 to 1.08 m/s to ensure a reasonable run time for the experiment. An iteration scheme to determine critical friction velocity has been done as outlined in [31] and [41]. For a constant free stream velocity, the critical friction velocity decreases for larger particles. With a constant particle diameter, the critical friction velocity decreases as the free stream velocity increases. The calculated critical friction velocity and predicted equilibrium thickness are validated using ANSYS Fluent for inlet velocity range from 0.6 to 1.08 m/s. It is concluded that the iteration scheme has accurately predict said parameters.

It was found from parametric studies that for a constant Re, as non-dimensional particle relaxation time increases, the particles take longer time to adjust themselves back to the fluid streamlines, resulting in a higher probability of being deposited on the wall. Hence, the non-dimensional deposition velocity increases with increase in non-dimensional particle relaxation time. The non-dimensional deposition velocity remains constant as Re increases due to increasing free-stream velocity and hydraulic diameter while maintaining a constant non-dimensional particle relaxation time because Re does not directly affect Brownian diffusion, eddy-impaction, and gravitational sedimentation.For a constant Re, as particle relaxation time increases, the deposition velocity increases, resulting in more particles being deposited over a unit area and time. In general, as more particles are deposited, the surface takes less time to become saturated and approach equilibrium faster. Therefore the saturation and equilibrium time decrease with increase in non-dimensional particle relaxation time. For a constant Re and non-dimensional particle relaxation time, the mass ratio of fluid and particles per unit volume increases, meaning fewer particles are presented per

unit volume, and fewer particles are deposited on the wall. As deposition velocity decreases, the time required to reach saturation increases. As the inlet velocity increases, the saturation and equilibrium time decreases for a constant particle concentration.

Calculations to predict the asymptotic deposition behavior of low-temperature, low-pressure experiments are conducted with air at 302K as the working fluid. The inlet velocity is varied at 0.6, 0.7, 0.8, 0.9, 1.0, and 1.08 m/s. As the inlet velocity increases, the saturation and equilibrium time decreases for the same particle concentration. For the inlet velocity above 1.08 m/s, there is no deposition happening as the critical friction velocity of 7.5 μm graphite particle is smaller than the shear velocity of the fluid and the thickness predicted is negative. For the same particle concentration, as the inlet velocity increases, asymptotic deposited mass decreases. It is easier to remove particles because the critical shear velocity is smaller for larger free stream velocity, with fewer particles being deposited; hence, smaller deposition mass.

5. CONCLUSIONS AND FUTURE WORK

Current plate-out codes predicting fission products and graphite dust transport are only accessible for internal institutional use and only apply to the nuclear application. However, porous particle deposition is crucial to many industrial heat recovery systems. The numerical findings based on the original geometry may be imprecise due to the accumulating deposition. The objective of this study is to develop a mathematical model for particle deposition in a fully developed turbulent flow in a rectangular channel considering the effect of the change in geometry over time due to particle deposition. The definitions of undersaturated, saturated, and equilibrium regions are introduced, along with saturation and equilibrium times. Equilibrium time can be expressed as a linear function of saturation time, which can be used to approximate one or the other with adequate given parameters. The most significant part of the study is to consider the particle-to-particle and particle-to-fluid interaction. Forces acting on the particle during the removal process are considered, including hydrodynamic torque, impact force, lift force, drag force, and 4 adhesion forces. A proposed experimental procedure to measure the total adhesion force has been suggested. Iteration schemes have been used to find critical friction velocity from [31] and equilibrium thickness. The results are validated by numerical simulation performed in ANSYS Fluent. It is concluded that the suggested methodology in this study is adequate to predict equilibrium thickness and critical shear velocity.

The following conclusions are drawn from the study:

- For a constant free stream velocity, the critical friction velocity decreases for larger particles. Smaller particles are harder to be removed by the fluid and free stream particles because hydrodynamic torque, drag force, lift force, and impact force is proportional to the particle's diameter. The fluid at the sublayer flow must have larger momentum to induce sufficient forces to remove smaller particles. With a constant particle diameter, the critical friction velocity decreases as the free stream velocity increases. As free stream particles carry more

momentum at higher free stream velocity, the impact force acting on adhered particles is larger. Therefore, the adhered particle is easier to remove, hence, lower critical shear velocity.

- For a constant Re, as non-dimensional particle relaxation time increases, the particles take a longer time to adjust themselves back to the fluid streamlines, resulting in more likelihood of being deposited on the wall. Hence, the non-dimensional deposition velocity increases with increase in non-dimensional particle relaxation time.

- The non-dimensional deposition velocity remains constant as Re increases due to increasing free-stream velocity and hydraulic diameter while maintaining a constant non-dimensional particle relaxation time because Re does not directly affect Brownian diffusion, eddy-impaction, and gravitational sedimentation.

- As particle relaxation time increases for a constant Re, deposition velocity increases, resulting in more particles deposited over a unit area and time. In general, as more particles are deposited, the surface takes less time to become saturated and approach equilibrium faster; hence, the saturation and equilibrium time decrease with increase in non-dimensional particle relaxation time.

- For a constant Re and non-dimensional particle relaxation time, the mass ratio of fluid and particles per unit volume increases, meaning fewer particles are presented per unit volume, and fewer particles are deposited on the wall. As deposition velocity decreases, the time required to reach saturation increases.

- For a constant particle concentration, as the inlet velocity increases, the saturation and equilibrium time decreases.

- For the inlet velocity above 1.08 m/s, there is no deposition happening as the critical friction velocity for 7.5 μm graphite particle is smaller than the shear velocity of the fluid and the thickness predicted is negative.

- As the inlet velocity increases, asymptotic deposited mass decreases for a fixed particle concentration. It is easier to remove particles because the critical shear velocity is smaller for larger free stream velocity, with fewer particles being deposited; therefore, smaller deposition mass.

Future work is needed to perform the adhesive force measurement by the AFM provided by MCF by Texas A&M. Adequate spring constant range should be further determined to perform future measurements. The porosity of the deposited porous sample also needs to be determined. The asymptotic deposition, saturation, and equilibrium time need further validation by running long-duration deposition at the suggested particle concentration and inlet velocity. For a constant free stream velocity, the critical friction velocity decreases for larger particles. Smaller particles are harder to be removed by the fluid and free stream particles because hydrodynamic torque, drag force, lift force, and impact forces are proportional to the particle's diameter. Therefore, the assumption of uniform diameter in the porous deposition layer and free stream particles might not be valid due to preferential deposition and removal, i.e., the average deposited particles' diameter could be smaller than the free stream ones. This study takes a two-dimensional, fully developed turbulent channel flow as a deposition geometry. For different deposition geometries, such as flow over a cylinder, a sphere, and transitional flow, Equation 3.50 needs to be modified to fit an appropriate configuration.

REFERENCES

[1] Z. Wu and Z. Zhang, "The advanced nuclear energy system and high-temperature gas-cooled reactor," 2004.

[2] T. D. Burchell and L. L. Snead, "The effect of neutron irradiation damage on the properties of grade nbg-10 graphite," *Journal of Nuclear Materials*, vol. 371, Jan. 2007. DOI: 10.1016/j.jnucmat.2007.05.021.

[3] M. Stempniewicz, L. Winters, and S. Caspersson, "Analysis of dust and fission products in a pebble bed ngnp," *Nuclear Engineering and Design*, vol. 251, pp. 433–442, 2012. DOI: 10.1016/j.nucengdes.2011.09.049.

[4] R. Moormann, "A safety re-evaluation of the avr pebble bed reactor operation and its consequences for future htr concepts," *Fourth International Topical Meeting on High Temperature Reactor Technology, Volume 2*, 2008. DOI: 10.1115/htr2008-58336.

[5] T. Lind, S. Guentay, A. Dehbi, Y. Liao, and C. Rycroft, "Psi project on htr dust generation and transport," Oct. 2010.

[6] Y. Zheng, M. M. Stempniewicz, Z. Chen, and L. Shi, "Study on the dlofc and plofc accidents of the 200 mwe pebble-bed modular high temperature gas-cooled reactor with tinte and spectra codes," *Annals of Nuclear Energy*, vol. 120, pp. 763–777, 2018. DOI: 10.1016/j.anucene.2018.06.041.

[7] W. Hudritsch and P. Smith, "Padloc: A one-dimensional computer program for calculating coolant and plateout fission product concentrations. [htgr]," 1977. DOI: 10.2172/5289739.

[8] O. Baba, N. Tsuyusaki, and S. K., "Fission products plate-out analysis code in the htgr," *Japan Atomic Energy Research Institute*, 1988.

[9] N.-i. Tak, J.-H. Lee, S. N. Lee, and C. K. Jo, "Posca: A computer code for fission product plateout and circulating coolant activities within the primary circuit of a high temperature gas-cooled reactor," *Nuclear Engineering and Technology*, vol. 52, no. 9, pp. 1974–1982, 2020. DOI: 10.1016/j.net.2020.02.006.

[10] R. Moormann, W. Schenk, and K. Verfondern, "Source term estimation for small-sized htgr: Status and further needs, extracted from german safety analyses," *Nuclear Technology*, vol. 135, no. 3, pp. 183–193, 2001. DOI: 10.13182/nt01-a3215.

[11] H. D. Jeong, "A study on transport behavior analysis of fission products in a vhtr," Ph.D. dissertation, Korea Advanced Institute of Science and Technology, 2019.

[12] Haas, "Radax-3-beschreibung," *HRB-Bericht EA 1347*, vol. 135, pp. 183–193, 1984.

[13] L. Stassen, "Validation of the plate-out model in the radax code used for plate-out and dust activity calculations at pbmr," *Advances in Nuclear Analysis and Simulation, PHYSOR*, pp. 2455–2464, 2006.

[14] J. S. Yoo, N.-i. Tak, H.-S. Lim, and J.-H. Chun, "Numerical prediction of the fission product plate-out for a vhtr application," *Annals of Nuclear Energy*, vol. 37, no. 4, pp. 471–481, 2010. DOI: 10.1016/j.anucene.2010.01.009.

[15] H. L. C. Yoon J.S. Yoo, "Preliminary theory manual for gamma-fp (fission products module of the transient gas multicomponent mixture analysis)," *Korea Atomic Energy Research Institute (KAERI)*, no. KAERI-TR-4933/2013, 2013.

[16] N.-i. Tak and C. Yoon, "Simulation of comedie fission product plateout experiment using gamma-fp," *Proceedings of the KNS 2014 Fall Meeting, Korea, Republic of: KNS*, no. KAERI-TR-4933/2013, 2013.

[17] Z.-X. Tong, M.-J. Li, Y.-L. He, and H.-Z. Tan, "Simulation of real-time particle deposition and removal processes on tubes by coupled numerical method," *Applied Energy*, vol. 185, pp. 2181–2193, 2017.

[18] D. Bouris and G. Bergeles, "Numerical calculation of the effect of deposit formation on heat-exchanger efficiency," *International Journal of Heat and Mass Transfer*, vol. 40, no. 17, pp. 4073–4084, 1997. DOI: 10.1016/s0017-9310(97)00058-6.

[19] B. A. Qureshi and S. M. Zubair, "The impact of fouling on performance of a vapor compression refrigeration system with integrated mechanical sub-cooling system," *Applied Energy*, vol. 92, pp. 750–762, 2012. DOI: 10.1016/j.apenergy.2011.08.021.

[20] B. A. Qureshi and S. M. Zubair, "The impact of fouling on the condenser of a vapor compression refrigeration system: An experimental observation," *International Journal of Refrigeration*, vol. 38, pp. 260–266, 2014. DOI: 10.1016/j.ijrefrig.2013.08.012.

[21] J. Tomeczek and K. Wacławiak, "Two-dimensional modelling of deposits formation on platen superheaters in pulverized coal boilers," *Fuel*, vol. 88, no. 8, pp. 1466–1471, 2009. DOI: 10.1016/j.fuel.2009.02.023.

[22] C. Paz, E. Suárez, A. Eirís, and J. Porteiro, "Development of a predictive cfd fouling model for diesel engine exhaust gas systems," *Heat Transfer Engineering*, vol. 34, no. 8-9, pp. 674–682, 2013. DOI: 10.1080/01457632.2012.738321.

[23] M. Andersson, J. Yuan, and B. Sundén, "Review on modeling development for multiscale chemical reactions coupled transport phenomena in solid oxide fuel cells," *Applied Energy*, vol. 87, no. 5, pp. 1461–1476, 2010. DOI: 10.1016/j.apenergy.2009.11.013.

[24] Q. Zheng, X. Li, Y. Cheng, G. Ning, F. Xing, and H. Zhang, "Development and perspective in vanadium flow battery modeling," *Applied Energy*, vol. 132, pp. 254–266, 2014. DOI: 10.1016/j.apenergy.2014.06.077.

[25] A. Masselot and B. Chopard, "A lattice boltzmann model for particle transport and deposition," *Europhysics Letters (EPL)*, vol. 42, no. 3, pp. 259–264, 1998. DOI: 10.1209/epl/i1998-00239-3.

[26] B. Chopard and A. Masselot, "Cellular automata and lattice boltzmann methods: A new approach to computational fluid dynamics and particle transport," *Future Gener. Comput. Syst.*, vol. 16, pp. 249–257, 1999.

[27] B. Chopard, A. Masselot, and A. Dupuis, "A lattice gas model for erosion and particles transport in a fluid," *Computer Physics Communications*, vol. 129, no. 1-3, pp. 167–176, 2000. DOI: 10.1016/s0010-4655(00)00104-1.

[28] N. Wood, "The mass transfer of particles and acid vapour to cooled surfaces," 1981.

[29] R. Chavez, D. Orea, B. Choi, *et al.*, "An experimental study of solid and liquid aerosol transport in a horizontal square channel," *Aerosol Science and Technology*, vol. 54, no. 12, pp. 1399–1423, 2020.

[30] T. R. Bott, *Fouling of heat exchangers*. Elsevier, 1995.

[31] C. Toscano and G. Ahmadi, "Particle removal mechanisms in cryogenic surface cleaning," *The Journal of Adhesion*, vol. 79, no. 2, pp. 175–201, 2003.

[32] Y.-Y. Quan, L.-Z. Zhang, R.-H. Qi, and R.-R. Cai, "Self-cleaning of surfaces: The role of surface wettability and dust types," *Scientific Reports*, vol. 6, no. 1, 2016. DOI: 10.1038/srep38239.

[33] A. Rifai, N. Abu Dheir, B. S. Yilbas, and M. Khaled, "Mechanics of dust removal from rotating disk in relation to self-cleaning applications of pv protective cover," *Solar Energy*, vol. 130, pp. 193–206, 2016. DOI: 10.1016/j.solener.2016.02.028.

[34] K. L. Johnson, A. D. Roberts, and K. Kendall, "Surface energy and the contact of elastic solids," *Proceedings of the Royal Society of London. A. Mathematical and Physical Sciences*, vol. 324, no. 1558, pp. 301–313, 1971. DOI: 10.1098/rspa.1971.0141.

[35] R. J. Isaifan, D. Johnson, L. Ackermann, B. Figgis, and M. Ayoub, "Evaluation of the adhesion forces between dust particles and photovoltaic module surfaces," *Solar Energy Materials and Solar Cells*, vol. 191, pp. 413–421, 2019.

[36] A. D. Zimon, *Adhesion of dust and powder*. [Online]. Available: https://link.springer.com/book/10.1007/978-1-4615-8576-3.

[37] B. Figgis and B. Brophy, "Pv coatings and particle adhesion forces," Oct. 2015.

[38] P. Lambert and J. Valsamis, "Axial capillary forces, surf. tens. microsc. eng. below capill. length," *Springer*, 2013. DOI: 10.1007/978-3-642-37552-1.

[39] Y. I. Rabinovich, J. J. Adler, M. S. Esayanur, A. Ata, R. K. Singh, and B. M. Moudgil, "Capillary forces between surfaces with nanoscale roughness," *Advances in Colloid and Interface Science*, vol. 96, no. 1-3, pp. 213–230, 2002. DOI: 10.1016/s0001-8686(01)00082-3.

[40] H. Choi, H. Kim, S. Hwang, W. Choi, and M. Jeon, "Dye-sensitized solar cells using graphene-based carbon nano composite as counter electrode," *Solar Energy Materials and Solar Cells*, vol. 95, no. 1, pp. 323–325, 2011. DOI: 10.1016/j.solmat.2010.04.044.

[41] M. Soltani and G. Ahmadi, "On particle adhesion and removal mechanisms in turbulent flows," *Journal of Adhesion Science and Technology*, vol. 8, no. 7, pp. 763–785, 1994. DOI: 10.1163/156856194x00799.

[42] G. Binnig, C. F. Quate, and C. Gerber, "Atomic force microscope," *Physical Review Letters*, vol. 56, no. 9, pp. 930–933, 1986. DOI: 10.1103/physrevlett.56.930.

[43] L. H. Segeren, B. Siebum, F. G. Karssenberg, J. W. Van Den Berg, and G. J. Vancso, "Microparticle adhesion studies by atomic force microscopy," *Journal of Adhesion Science and Technology*, vol. 16, no. 7, pp. 793–828, 2002. DOI: 10.1163/15685102760136418.

[44] B. Derjaguin, V. Muller, and Y. Toporov, "Effect of contact deformations on the adhesion of particles," *Journal of Colloid and Interface Science*, vol. 53, no. 2, pp. 314–326, 1975. DOI: 10.1016/0021-9797(75)90018-1.

[45] D. Maugis, "Adhesion of spheres: The jkr-dmt transition using a dugdale model," *Journal of Colloid and Interface Science*, vol. 150, no. 1, pp. 243–269, 1992. DOI: 10.1016/0021-9797(92)90285-t.

[46] H. Hamaker, "The london—van der waals attraction between spherical particles," *Physica*, vol. 4, no. 10, pp. 1058–1072, 1937. DOI: 10.1016/s0031-8914(37)80203-7.

[47] V. A. Parsegian, *Van der waals forces: A handbook for Biologists, chemists, engineers, and physicists*. Cambridge University Press, 2006.

[48] L. Olsson, P. Tengvall, R. Wigren, and R. Erlandsson, "Interaction forces between a tungsten tip and methylated sio2 surfaces studied with scanning force microscopy," *Ultramicroscopy*, vol. 42-44, pp. 73–79, 1992. DOI: 10.1016/0304-3991(92)90248-i.

[49] R. Jones, H. M. Pollock, J. A. Cleaver, and C. S. Hodges, "Adhesion forces between glass and silicon surfaces in air studied by afm: effects of relative humidity, particle size, roughness, and surface treatment," *Langmuir*, vol. 18, no. 21, pp. 8045–8055, 2002. DOI: 10.1021/la0259196.

[50] M. Gotzinger and W. Peukert, "Dispersive forces of particle–surface interactions: Direct afm measurements and modelling," *Powder Technology*, vol. 130, no. 1-3, pp. 102–109, 2003. DOI: 10.1016/s0032-5910(02)00234-6.

[51] e. Gauthier, e. Alvo, o. Dejeu, B. Tamadazte, P. Rougeot, and Regnier, "Analysis and specificities of adhesive forces between microscale and nanoscale," *IEEE Transactions on Automation Science and Engineering*, vol. 10, no. 3, pp. 562–570, 2013. DOI: 10.1109/tase.2013.2248150.

[52] H.-J. Butt, B. Cappella, and M. Kappl, "Force measurements with the atomic force microscope: Technique, interpretation and applications," *Surface Science Reports*, vol. 59, no. 1-6, pp. 1–152, 2005. DOI: 10.1016/j.surfrep.2005.08.003.

[53] L. O. Heim, S. Ecke, M. Preuss, and H.-J. Butt, "Adhesion forces between individual gold and polystyrene particles," *Journal of Adhesion Science and Technology*, vol. 16, no. 7, pp. 829–843, 2002. DOI: 10.1163/156856102760136427.

[54] M. Götzinger and W. Peukert, "Particle adhesion force distributions on rough surfaces," *Langmuir*, vol. 20, no. 13, pp. 5298–5303, 2004. DOI: 10.1021/la049914f.

[55] N. M. Mokgalapa, T. K. Ghosh, and S. K. Loyalka, "Graphite particle adhesion to hastelloy x: Measurements of the adhesive force with an atomic force microscope," *Nuclear Technology*, vol. 186, no. 1, pp. 45–59, 2014. DOI: 10.13182/nt13-9.

[56] W. A. Ducker, T. J. Senden, and R. M. Pashley, "Measurement of forces in liquids using a force microscope," *Langmuir*, vol. 8, no. 7, pp. 1831–1836, 1992. DOI: 10.1021/la00043a024.